Master thesis and internship[BR]- Master's Thesis : Deterministic model construction for flutter characterisation of cantilever flat plates[BR]- Internship (linked to master's thesis)

Auteur : Oleffe, Thomas
Promoteur(s) : Dimitriadis, Grigorios
Faculté : Faculté des Sciences appliquées
Diplôme : Master en ingénieur civil en aérospatiale, à finalité spécialisée en "aerospace engineering"
Année académique : 2019-2020
URI/URL : http://hdl.handle.net/2268.2/10270

LIÈGE université

Deterministic model construction for flutter characterisation of cantilever flat plates

Master thesis conducted by

Oleffe Thomas

in the purpose of obtaining the Master's degree in Aerospace Engineering

Promoter

Prof. Greg Dimitriadis

Jury members

Dr. Thomas Andrianne

Prof. Vincent E. Terrapon

University of Liège

Faculty of Applied Sciences

Acknowledgement

I would like to show my gratitude to my promoter Prof. Greg Dimitriadis who proposed me this work that is not a topic we have been used to in the Master in Aerospace. It has been very motivational to work on new concepts that were a priori unknown to me and to apply them in this specific context. Furthermore, the possibility to perform practical tests at the wind tunnel to finally see what it gives in reality as well as his motivation and his interest for the subject have encouraged me to keep going.

I also wish to thank Dr. Thomas Andrianne for his advices concerning all the practical aspects of the work, from the design of the excitation sytem to the wind tunnel tests. indeed, it has been a very good exercise for me to think from both a practical and a theoretical point of view at the same time. I am now a little more confident about how to carry out a project from the theoretical ideas to its realisation in practice.

I also thank my friend Xavier Naa for the many talks we had that helped me seeing my work from an external point of view that allowed me to go further in my investigation.
I would like to thank my partner, my friends and my family who always showed me their support for giving the best of myself. I have learned a lot from having them by my side and I hope that it is only the beginning.

Finally, I would thank the professors we have had for all those years that showed us their interest for what they love, trying to share everything they could with us and always worrying to know if everything was alright. Thank you for your time and interest.

Nomenclature

Λ quarter-chord sweep angle (°) or (rad)

λ Taper ratio (-)

ε Residual between the observed and the fitted flutter indices (-)

ζ Damping ratio (-)

AR Aspect ratio (-)

b Half-root chord (m)

c_r Wing root chord (m)

c_t Wing tip chord (m)

f_f Flutter frequency (Hz)

$k = \dfrac{\omega b}{V_\infty}$ Reduced frequency (-)

m Number of independent variables (-)

MSE Mean squared error (-)

n Number of experiments (-)

p Number of model's parameters (-)

R^2 Multiple correlation coefficient (-)

S Wing surface (m^2)

s Wing span (m)

SSE Sum of the squares of the errors (-)

SST Total sum of squares (-)

V_f Flutter velocity (m/s)

V_f^* Flutter index (-)

Abstract

Assessing exactly the flutter speed and frequency is of prior importance when designing an aircraft to ensure a safe flight envelope and to this purpose, experimental and numerical tests have been developed throughout the years. To simplify the computation of the critical speed and frequency, this master thesis proposes to build a mathematical model for flutter characterisation as a function of geometrical parameters of cantilever flat plates namely the Aspect Ratio, the taper ratio and the sweep angle, on the basis of the unsteady Vortex Lattice Method (VLM). The investigation of the hump mode activation as a function of those parameters is carried out in first place to assess its conditions of appearance and it is concluded that a straight discontinuity line can be drawn on the domain to distinguish the zone where the hump is active from the zone where it is not. Then, the linear regression theory is used for building the model and three different polynomial orders are compared. and conclusion is made that a incomplete second order model provides results reliable up to 99%. A comparison is made with experimental results obtained in wind tunnel. To do so, an excitation system is designed so that its eigenfrequencies do not interfere with those of the tested plates. Several issues encountered due to lack of time because of the sanitary crisis prevented to perform more than two tests for which the different problems could not all be checked and solved. In the end, a proper conclusion about the practical validity of the model could not be drawn.

Table of contents

List of Figures

List of Tables

1 Introduction

1.1 Problem definition

Flutter is an aeroelastic phenomenon that results from an unfavorable interaction between the aerodynamic, elastic and structural forces that causes undamped oscillations often leading to structural failure. Such a phenomenon appeared in the early 1920s with the increase of aircraft speed and from then, characterising the flutter has been of prior importance in the design of aircraft. At this time, no proper flutter tests existed and the aircraft was simply flown to cover the whole flight envelope to ensure that it was flutter free. The first flutter test was created in 1953 by Von Schlippe and it consisted in vibrating the aircraft at its eigenfrequencies, starting at low speed and then increasing progressively. The response amplitude was measured and plotted as a function of the airspeed. when this amplitude was becoming high enough suggesting a very low or even a null damping, the flutter speed was obtained [1]. Throughout the years, the flutter tests quality has improved until eventually coming to a numerical characterisation of the phenomenon. Simplifying the process to get an accurate estimation of the flutter properties is therefore very appreciated to avoid risks of failure and costly simulations.

Several types of flutter exist depending on the application and on the configuration that is considered. In this master thesis, focus is made on the most common one that aircraft can encounter, namely the wing bending-torsion flutter. As the name suggests, the phenomenon involves both the bending and torsion modes of the wing which combine to extract the energy from the free stream and create the flutter phenomenon when the critical speed is reached. At this specific speed, the energy extracted from the free stream is exactly dissipated so that the motion amplitude remains constant but when going for higher speeds, the whole energy is not dissipated increasing the motion of the wing until structural failure. The motion of the wing is shown in Fig. 1, the wing flaps up and down and rotates at the same time around its rotation axis.

As flutter is an aeroelastic phenomenon, it combines inertial, structural and aerodynamic forces that are directly impacted by the geometry of the structure. It is therefore expected that the flutter speed and frequency greatly depend on the geometry and characterizing this dependency becomes of prior interest in the design of aircraft. Furthermore, this would bring the flutter characterisation back to the earliest stages of the design which can be very interesting. The goal of this master thesis is thus to provide a mathematical model that relates the flutter speed and frequency to
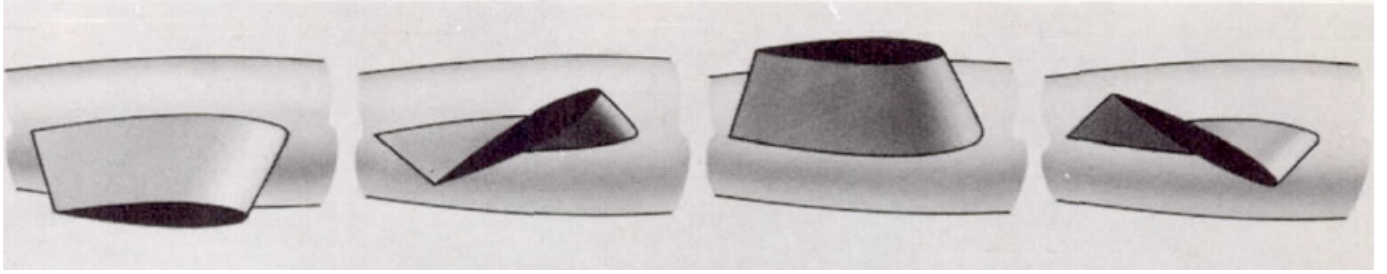
Figure 1: Wing bending-torsion flutter [2]

geometrical parameters of a wing. A wing's geometry is fully described by several parameters that are the camber, the thickness, the span, the root and tip chords and the sweep angle. However, some simplifying assumptions are made.

- No camber is considered.

- Only flat plates are considered. Given that it is impossible to get plates that are infinitely thin, a constant thickness of 0.001m is imposed in the modelling process.

- The plates are expected to be fixed on an excitation system for wind tunnel experiments so that the root chord is set to a constant $c_{\text{root}} = 0.2$m.

- Only geometric dependency is investigated here, the material is set to be aluminium for all the plates, with the following properties

Density ρ	2,700 kg/m³
Young modulus E	70,000 MPa
Poisson ratio ν	0.33

Table 1: Aluminium mechanical properties of the plates.

After those simplifications, the parameters that remain are the span, the tip chord and the sweep angle. To get rid of the units, dimensionless parameters are used namely the aspect ratio, the taper ratio and the quarter-chord sweep angle expressed in radians in the model.

$$\lambda = \frac{c_{\text{t}}}{c_{\text{r}}} \tag{1}$$

$$AR = \frac{s^2}{S} = \frac{s^2}{\frac{1}{2} \cdot b(c_{\text{r}} + c_{\text{t}})} = \frac{2s}{c_{\text{r}}(1 + \lambda)} \tag{2}$$

Note that in this context, cantilever plates are modelled so that the aspect ratio corresponds to that of a half-wing and must be doubled to get the aspect ratio that would exhibit a full wing.

Throughout this thesis, nondimensional independent variables are used. The flutter speed and frequencies being respectively expressed in m/s and Hz, the results are shown under the form of a flutter index defined as

$$V_f^* = \frac{V_f}{f_f \, b} \tag{3}$$

so that units mismatch issues are avoided.

1.2   Vortex Lattice Method

The numerical results used to build the mathematical model are obtained using a modal frequency domain version of the Vortex Lattice Method (VLM) in an unsteady configuration described in [4] based on the work proposed by Katz and Plotkin in [3]. The general procedure consists in solving the modal aeroelastic equations written on the basis of Lagrange's equation

$$\frac{d}{dt}\left(\frac{\partial L}{\partial \dot{r}_i}\right) - \frac{\partial L}{\partial r_i} = Q_i \tag{4}$$

where $L = T - V$ is the total energy of the structure, r_i is the ith generalised coordinate and Q_i is the generalised aerodynamic force term.

As shown in Fig. 2, the wing is flattened on its camber surface and geometrical panels are used to discretise the structure. On each of those panels, vortex rings with circulation Γ are imposed so that their leading edge corresponds to the quarter-chord of the panel. The wake is also paneled up to enforce the unsteady Kutta condition and its influence on the wing is computed through the use of influence coefficients. The goemetries of both the wing and its wake remain the same for the whole time history and the out-of-plane structural motion is modelled using downwash term in the aerodynamic loads on the basis of the structural mode shapes obtained using a FE model. Note that the in-plane motions are not considered. The mode shapes are interpolated on the control points located at the center of each vortex ring, i.e. on the three-quarter-chord of each aerodynamic panel so that it matches with the aerodynamics discretisation on the basis of which the aerodynamic loading is computed.
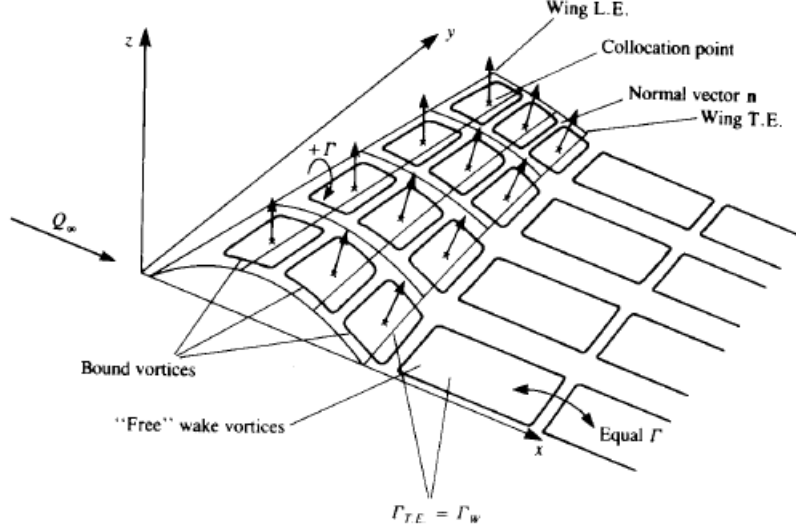
Figure 2: Illustration of the aerodynamic discretisation of the wing from reference [3].

Starting from the general equation 4, the impermeability and Kutta conditions are enforced and following the mathematical developments proposed in [4], the complete set of modal aeroelastic equations is obtained under the matrix forme as

$$\mathbf{A}\ddot{\mathbf{r}} + \mathbf{E}\mathbf{r} = \mathbf{Q}(t) \tag{5}$$

with $\mathbf{A}$ and $\mathbf{E}$ respectively the modal mass and stiffness matrices corresponding to mode shape $\mathbf{W}_i$.

In the frequency domain, the modal equations become

$$\left(-\left(\frac{kQ_\infty}{b} \right)^2 \mathbf{A} + \mathbf{E} - \rho Q_\infty^2 \mathbf{Q}_1(k) \right) = -\rho Q_\infty^2 \mathbf{Q}_0(0) \tag{6}$$

with $\mathbf{Q}_0(0) = \left(\mathbf{L}_0(0)^{\mathrm{T}} \mathbf{W} \right)^{\mathrm{T}}$ and $\mathbf{Q}_1(k) = \left(\mathbf{L}_1(k)^{\mathrm{T}} \mathbf{W} \right)^{\mathrm{T}}$.

The flutter speed and frequencies are finally obtained by setting the flutter determinant to zero

$$\det\left(-\left(\frac{k_{\mathrm{f}} Q_{\mathrm{f}}}{b} \right)^2 \mathbf{A} + \mathbf{E} - \rho Q_\infty^2 \mathbf{Q}_{\mathrm{f}}(k_{\mathrm{f}}) \right) = 0 \tag{7}$$

In practice, the determination of the conditions under which the flutter determinant becomes zero is made using a Newton-Raphson procedure. This requires to select initial values of speed and reduced frequency that are near the exact solution to ensure a rapid and correct convergence. Furthermore, a certain amount of information is needed for the method to provide the expected results. Even though the bending-torsion flutter involves the first three vibration modes, at least five of them must be provided to the VLM code for the results to be reliable.

4

2 Numerical simulations

This section is dedicated to the numerical part of the work on which the model is built comprising the Finite Elements (FE) and aeroelastic modelling of the plates. Also, the selection of the model is proposed after having analysed the results and investigated the presence of hump modes.

2.1 Design domain

The first task to achieve is the selection of the initial set of geometrical parameters. The purpose is to create a mathematical model that best reflects reality so that a certain number of simulations must be carried out. Continuous variables are considered and the number of configurations can become enormous which is prohibited. It is necessary to find a moderate sized set of initial values that provides as much information as possible.

The bounds of the domain are selected in first place so that a rather large field is covered that comprises many of the classical aircraft wings configurations

- AR: as mentioned above, the aspect ratios considered here correspond to cantilever plates. Setting the bounds to $AR_{\min} = 2$ and $AR_{\max} = 5$ therefore corresponds to the domain from 4 to 10 for a full wing.

- taper ratio: most of the time, the taper ratio is comprised between 0 for delta wings and 1 for rectangular ones with some exceptions going above 1. The taper ratio's bounds are set to be $\lambda_{\min} = 0.25$ and $\lambda_{\max} = 1$.

- quarter-chord sweep angle: no forward-swept wings are considered so that the lower bound is $\Lambda_{\min} = 0°$. The upper bound is set arbitrarily to $\Lambda_{\max} = 30°$.

For exploring the domain uniformly, each factor is divided into four levels which creates orthogonal grids that generate the cubic domain presented in Fig. 3 corresponding to the 64 plates presented in Fig. 4.
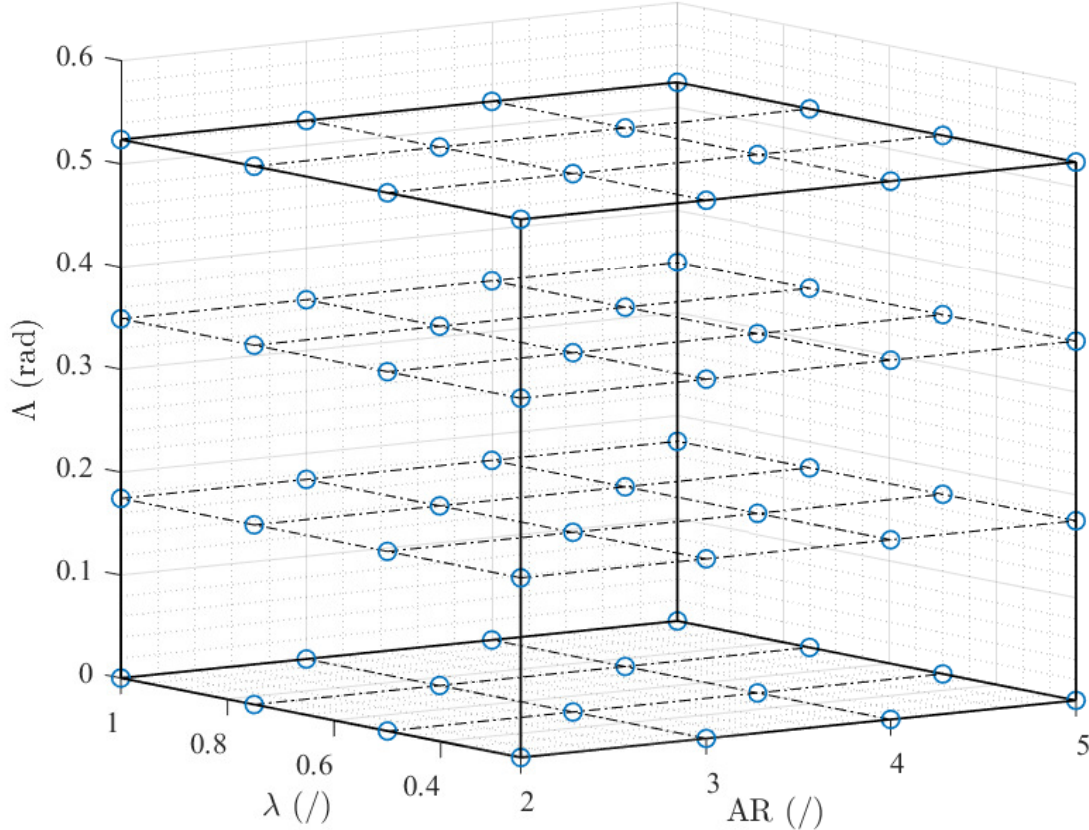
Figure 3: Design domain.

2.2 Structural analysis

The UVLM requires the modal mass and stiffness matrices of each plate as well as the eigenmodes. Those information are obtained using the FEA solver NASTRAN available in the SIEMENS NX software. The data are then extracted and written under the desired format using MATLAB as described in the Appendix. FE models of the plates have to be constructed and the question arises about the type and number of elements to be used for the solver to provide accurate results.

The plates are all 1 mm thick making the use of shell elements adapted to the situation. Additionally, only linear structural problems are considered and no curvature exists in the plates models. Having a mid-side node on each element does not present any real advantage and is expected to make the computation more costly even though the models are quite simple. Finally, the triangular elements generally present the drawback to be too much stiff in bending when used in small number. This number is expected not to be too high for making both the the structural and aeroelastic analyses of the 64 plates not too much time costly so that using triangular elements is probably
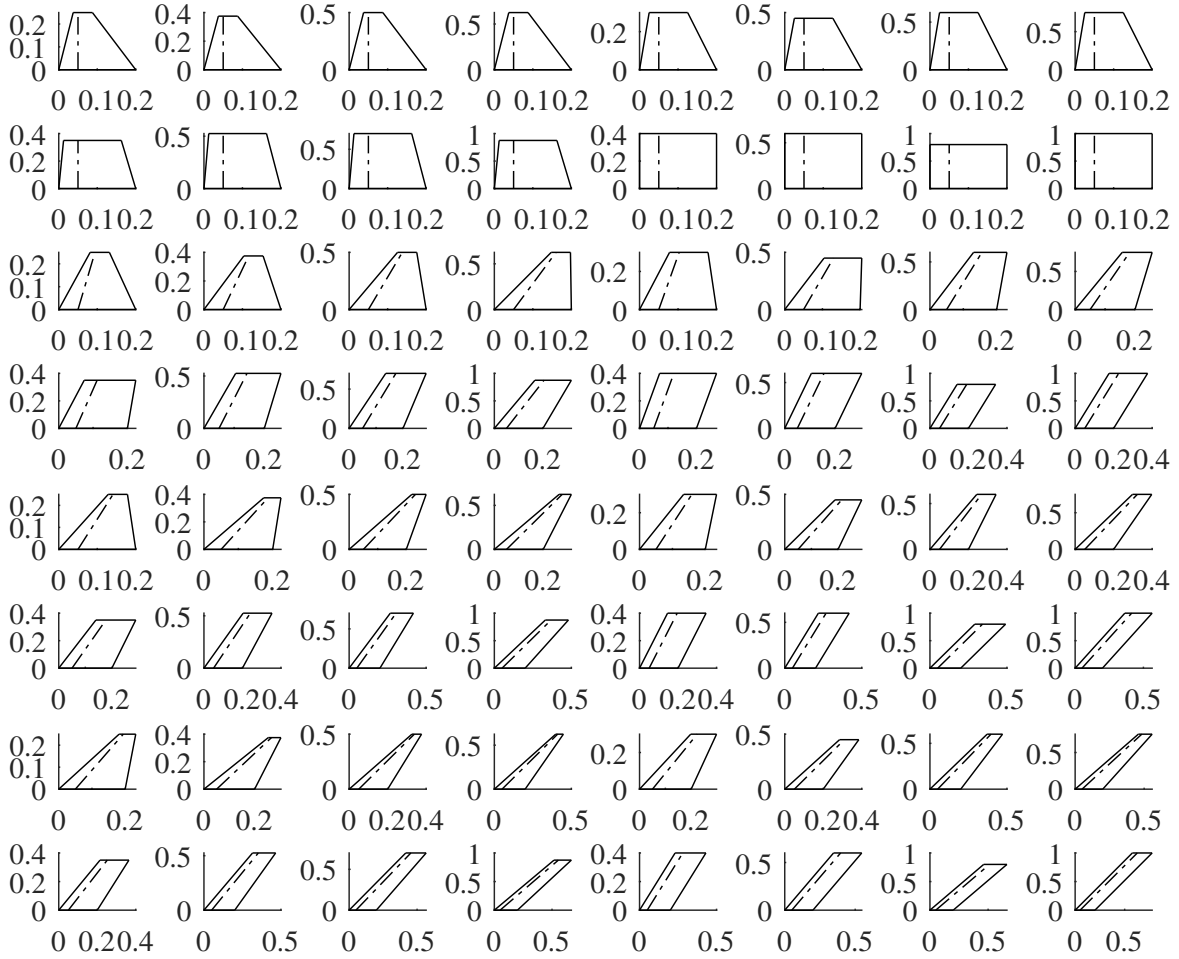
Figure 4: Representation of the 64 plates obtained with the orthogonal design domain.

not adapted for the present application. Given that bending modes are of interest, the choice is made to use CQUAD4 elements in a structured mesh. The modal analysis is then achieved using the "SOL 103 Real eigenvalues" solution type proposed by NASTRAN and the root chord is fixed to create the clamping boundary condition of cantilever plates.

The discretisation in finite elements is investigated on the plate having the smallest surface i.e. the most rigid one corresponding to the plate 1. A convergence study of the eigenfrequencies computed with NX NASTRAN is performed in terms of the elements size and presented in fig. 5. The upper graph shows the evolution of the frequencies as the size decreases until 1mm. The lower one depicts the relative difference with the results obtained at size 1mm. When reaching 5mm, the maximum relative difference is obtained for the 5th frequency and is of order 0.1%. It is concluded that con-

vergence has been achieved.
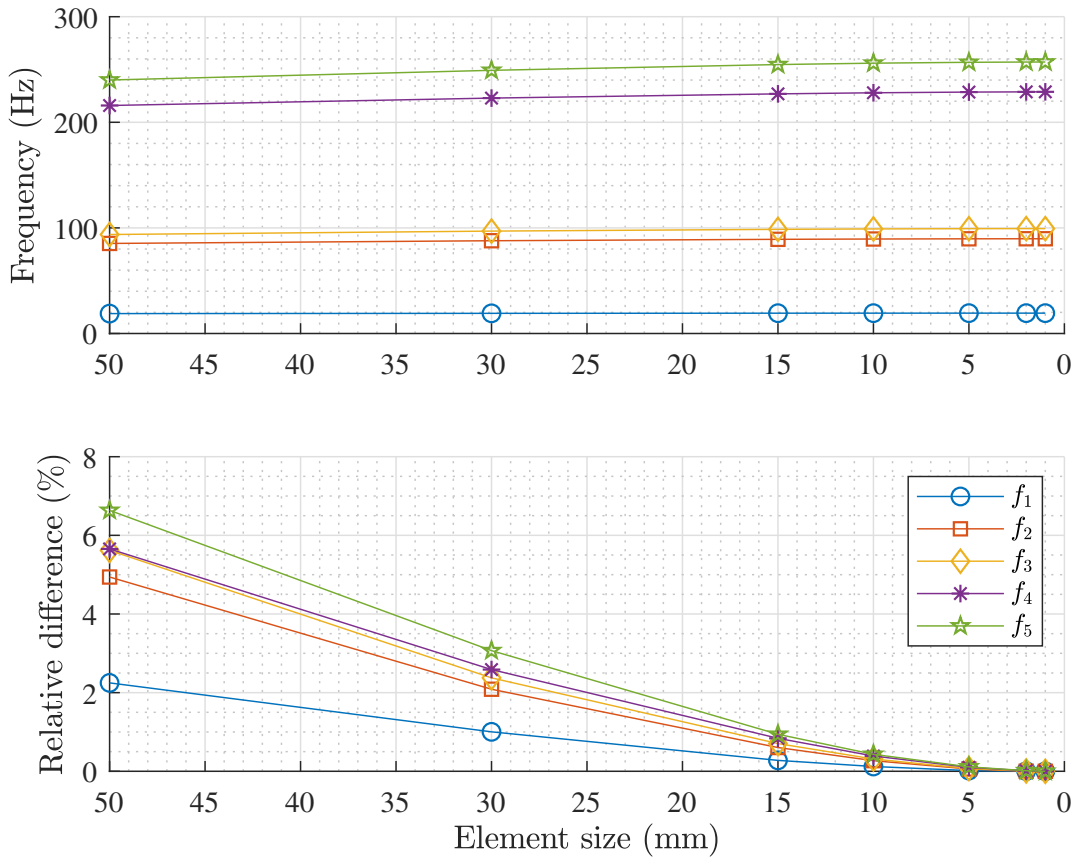
Figure 5: Structural convergence study of the five first eigenfrequencies of plate 1 in terms of the elements size.

However, for the sake of simplicity in the extraction of the stiffness and mass matrices and the eigenmodes, it could be useful to get the same number of nodes, i.e. the same number of elements for each plate. having 5mm elements on plate 1 corresponds to 2200 elements or again 40 elements chordwise and 55 elements spanwise. A similar convergence study is achieved on the plate having the largest surface i.e. the plate 16, to verify that 2200 elements are enough to provide accurate results. The variation of the first five eigenfrequencies in terms of the number of elements this time is presented in Fig. 6.
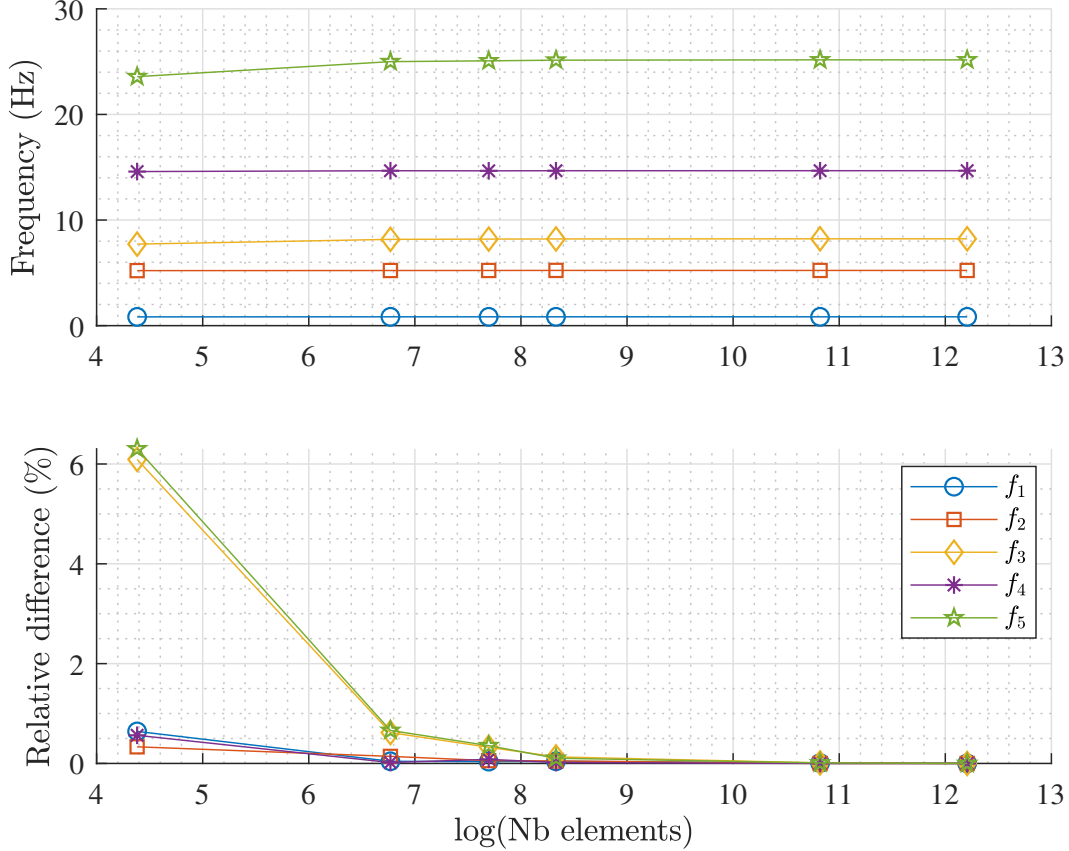
Figure 6: Structural convergence study of the five first eigenfrequencies of plate 16 in terms of the number of elements.

As for plate 1, the frequencies are provided in the upper graph while the lower one presents the relative difference with the frequencies obtained for 1mm elements (200,000 elements). With 2200 elements the maximum relative difference is again obtained for the 5th frequency and is of order 0.35%. It is therefore assumed that 2200 elements are sufficient to obtain accurate results for all the plates.

Fig.7 depicts the variation of the wind-off natural frequencies as a function of the selected parameters. It shows that the frequencies do almost not depend on the sweep angle. For a constant span and tip chord, i.e. constant aspect and taper ratios, sweeping the wing back slightly increases its mass and decreases its stiffness. As a result, the eigenfrequencies decrease very slightly with the sweep angle at the point of appearing almost constant over the range of values considered. Nevertheless, the two other parameters are affecting more importantly the obtained values. The aspect ratio is the one having the greatest impact. The longer the plate the earlier in frequency it

vibrates given that its rigidity decreases greatly while its mass increases. Both effects combine to rapidly lower the wind-off frequencies. Similarly, the taper ratio modifies both the mass and the stiffness of the structure. the higher the taper ratio, the higher the mass and the lower the stiffness and again, both effects combine but to a lesser extent.
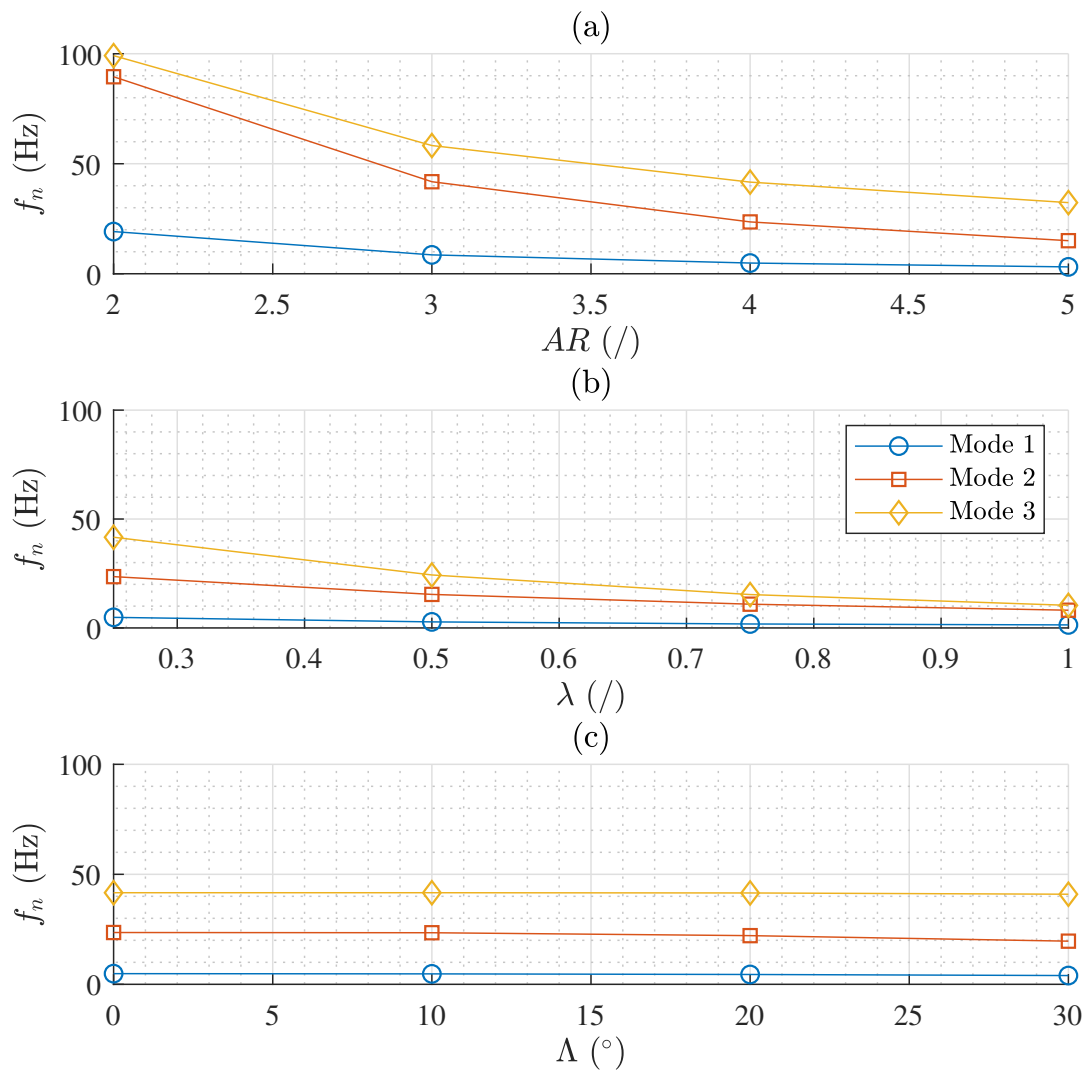
Figure 7: Variation of the first three natural frequencies as a function of the three geometrical parameters. (a) $\lambda = 0.25$, $\Lambda = 0°$; (b) $AR = 4$, $\Lambda = 0°$; (c) $AR = 4$, $\lambda = 0.25$.

The 64 plates are modelled using 40 chordwise and 55 spanwise finite elements and Tab.2 illustrates the FE discretisation and the first five eigenmodes of plate 1.

FE discretisation	mode 1, $f_1 = 19.28$ Hz	mode 2, $f_2 = 89.66$ Hz
mode 3, $f_3 = 99.25$ Hz	mode 4, $f_4 = 228.61$ Hz	mode 5, $f_5 = 256.81$ Hz
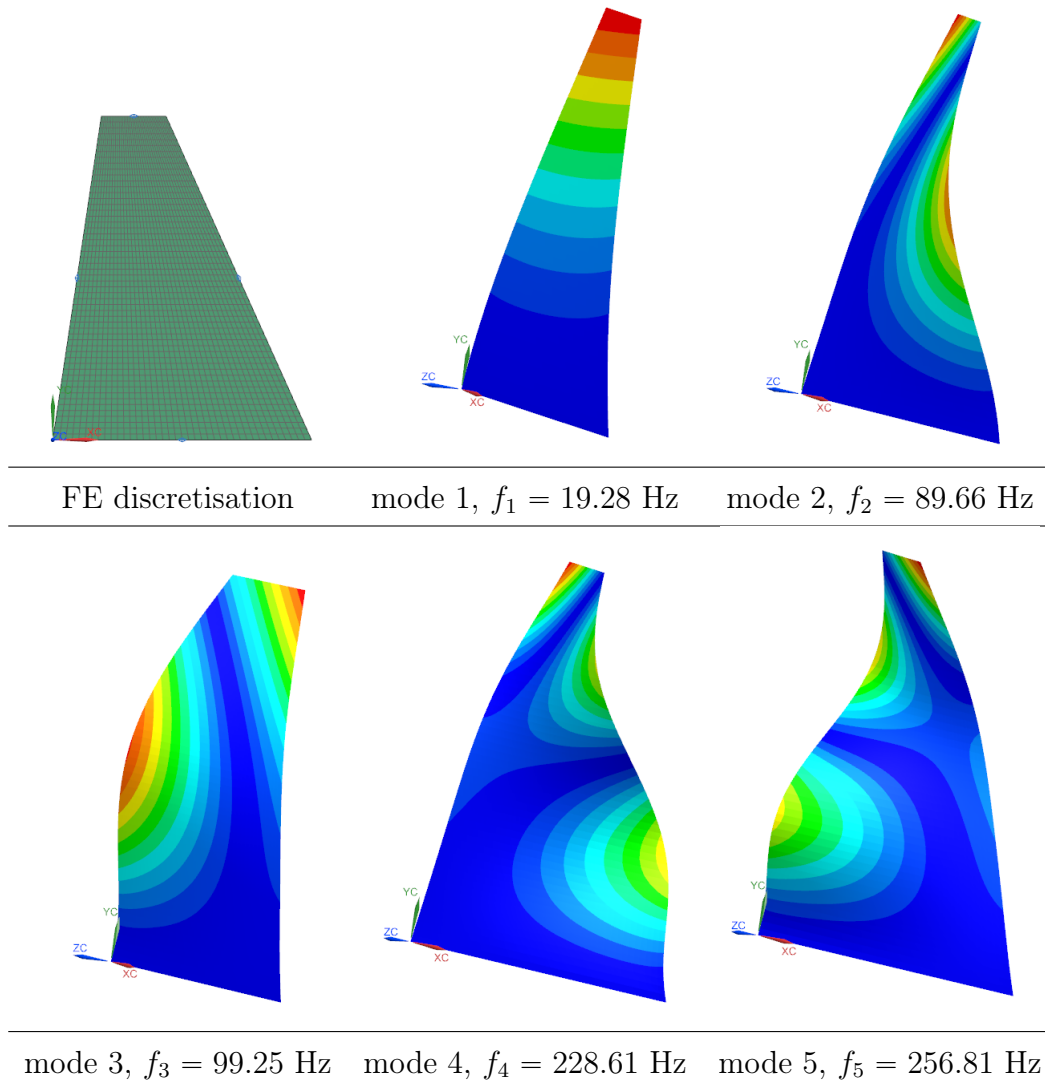
Table 2: Modal analysis of plate 1.

2.3 Aeroelastic analysis

To solve the generalised aeroelastic force matrix problem, the plates are divided into m chordwise and n spanwise aerodynamic panels and the aeroelastic results depend on this discretisation.

First of all, the convergence proposed in [4] is made with a sine distribution of the spanwise panels. Here, a linear distribution is used trying to match with the structural discretisation for allowing a better interpolation of the mode shapes on the aerodynamic mesh. Indeed, having more aerodynamic panels than structural ones is meaningless and can result in bad interpolation so that the finest resolution that can be achieved a priori is $m_{max} = 40$ and $n_{max} = 55$. The VLM method mirrors the plate around its root chord aiming to set up a symmetric flowfield. The spanwise number of aerodynamic panels is therefore twice that of the structural panels which gives $n_{max} = 110$.

The number of chordwise aerodynamic panels is set exactly the same way as the structural ones (along the root chord) so that selecting the maximum allowable value does not cause any trouble in the results. Concerning the number of spanwise panels, the number of finite elements have been imposed along the leading edge that is swept while the number of aerodynamics panels is set along the span that is a pure vertical line and mismatch can therefore occur between structural and aerodynamic panels. Analysing the convergence of the results before selecting a spatial resolution is thus necessary. Fig. 8 shows that when reaching $n = 100$, the results stop following the convergence curve. This issue is explained because the two discretisations are not made the same way. The structural panels have been imposed along the leading edge that is swept back while the aerodynamic ones are imposed along the span that is not swept. Because of this, when refining the VLM mesh too much i.e. when its number of elements becomes close to that of the structural mesh, the aerodynamic panels are becoming smaller than the structural ones in the spanwise direction. This does therefore lead to the problem of having two aerodynamic panels for a single finite element one resulting in a bad interpolation ([4]).

With this issue being highlighted, the most converged results are obtained for $n = 90$ for the selected FE discretisation and the relative difference is computed with respect to those results for the plates 1 and 16.

For $n = 70$, this difference is of order 0.48% for the plate 1 and 0.63% for the plate 16 while the computation times are respectively 74.4s and 86.8s. Taking into account that the computation time grows exponentially and that 64 plates are expected to be modelled, it has been decided to not spend too much time for slightly getting closer to the most converged value and the number of spanwise aerodynamic panels has been set to $n = 70$ for all the plates. Note that a refinement of
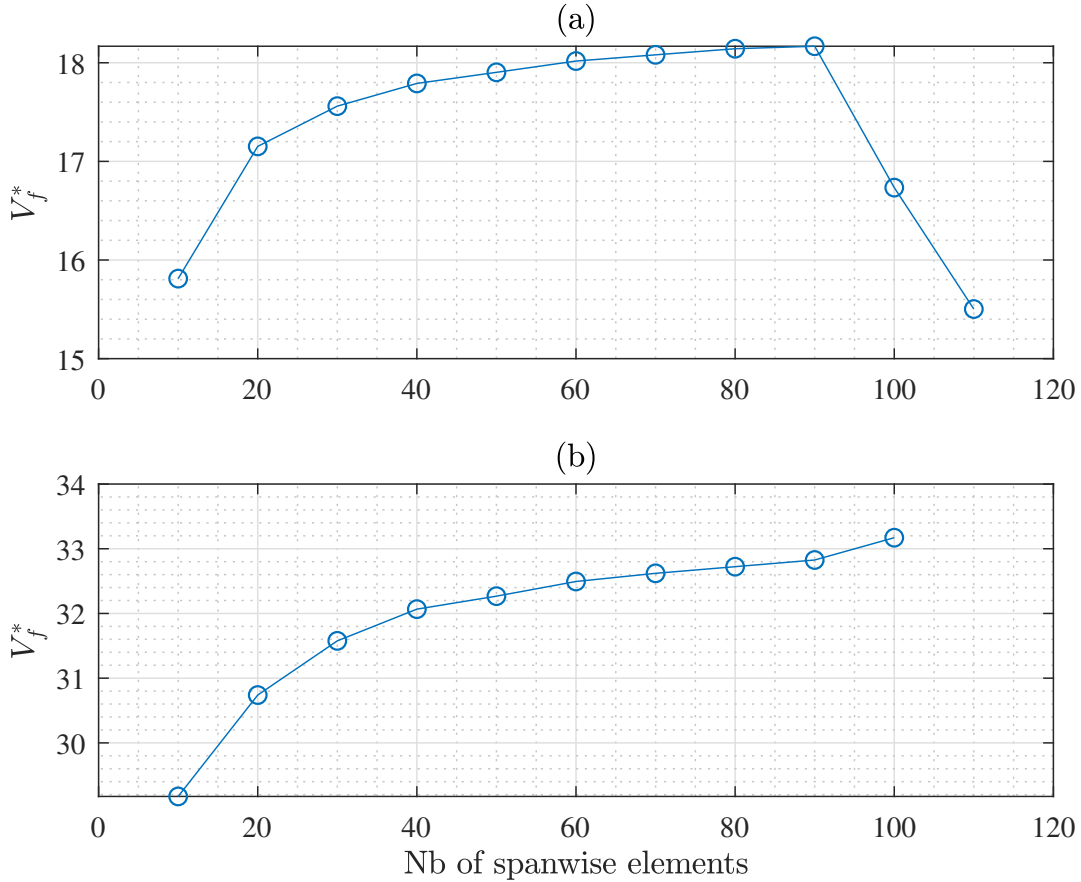
Figure 8: Aerodynamic convergence study in terms of spanwise elements linearly distributed. (a) variation of the flutter index for plate 1; (b) variation of the flutter index for plate 16.

the mesh could be carried out but it must be done in parallel with the refinement of the structural mesh to avoid any possible interpolation error between the two meshes.

2.4 Flutter index model construction

The model developed in this work is called a black box model meaning that the goal is to relate the output to the input with an empirical law on the basis of the experiments. No real use is made of the physics of the phenomenon to build the prediction law. The objective is therefore to fit a set of surfaces to the numerical flutter index data that depend on the Aspect ratio, the taper ratio and the quarter-chord sweep angle with the physical properties of the material, the thickness and the root chord that are kept constant for all the cases.

Until now, nothing is known a priori on the form of the equation that best fits the numerical results. The first objective is therefore to investigate the dependency of the phenomenon on the selected

factors, also called independent variables, to determine whether a linear or nonlinear law in terms of the model's parameters has to be used. Then, the quality of the model is assessed and an analysis of each term's necessity is eventually proposed leading to a simpler law with an acceptable level of accuracy.

It is important to mention that all the mathematical development proposed here has been obtained with the sweep angle being expressed in radians.

2.4.1 VLM results

As mentioned earlier, the flutter phenomenon considered here is an interaction between bending and torsion modes so that only the damping curves corresponding to those modes are of interest. To illustrate the typical results obtained with the VLM, the curves are provided in Fig.9 for plate 1.
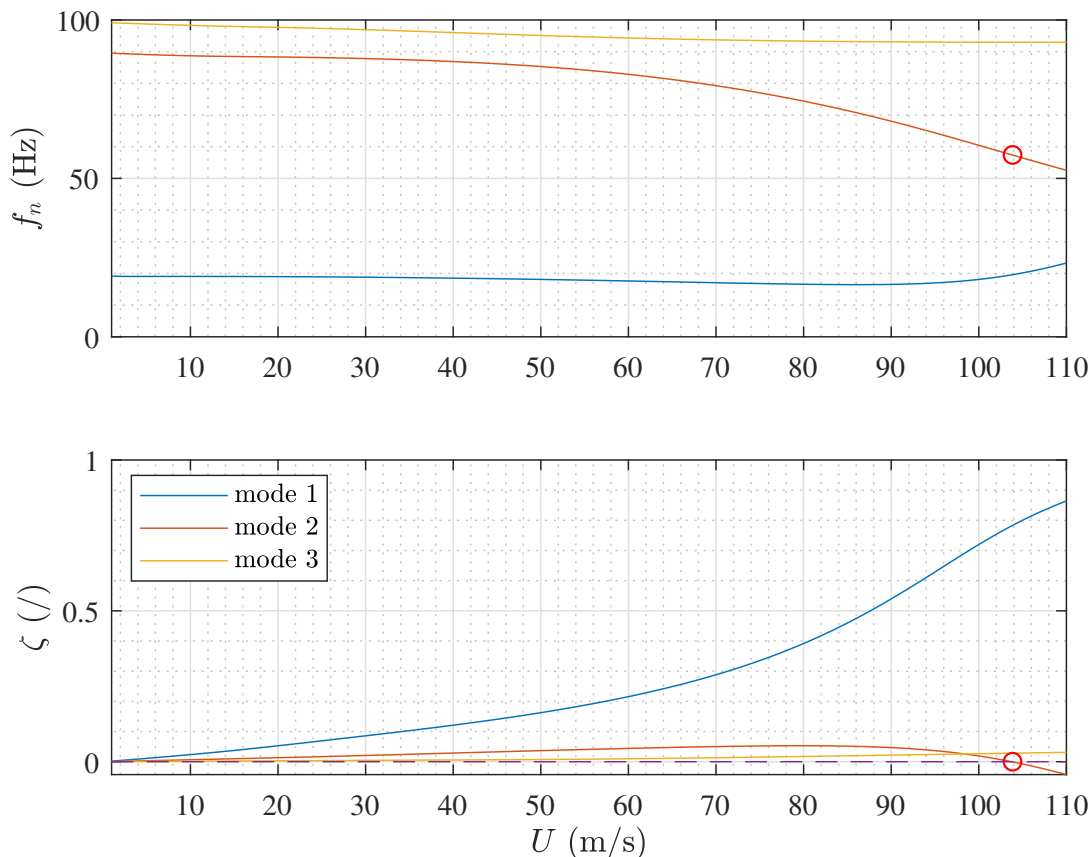
Figure 9: Frequency and damping curves for the first three modes obtained with VLM for plate 1.

The critical flutter speed and frequency are obtained when the damping curve crosses the zero axis meaning that the aerodynamic damping perfectly counterbalances the structural one so that

the total damping becomes zero preventing the motion amplitude to decrease. Going for higher airspeed makes the aerodynamic damping greater and the total damping becomes negative which has the consequence to amplify any vibration occurring in the structure until it breaks.

Following the definition proposed in Eq.3, the 64 flutter indices are obtained and shown in Fig.10.
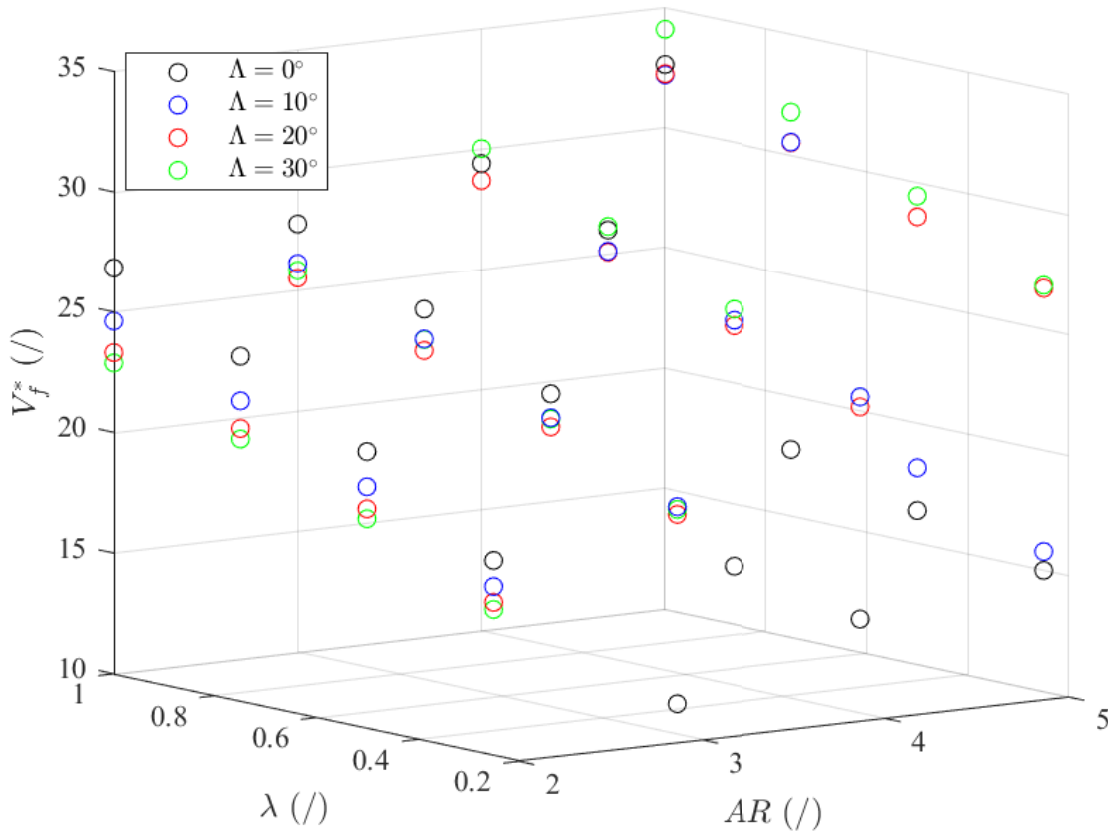
Figure 10: Flutter indices obtained for the 64 plates and shown for each level of sweep angle.

It appears that for $\Lambda = 20°$ and $30°$, the results follow a smooth increasing tendency as the aspect and taper ratios both increase. For the two lower levels of sweep angle, the same tendency is observed on a portion of the domain only. Indeed in a zone, that is different in both cases, where the aspect ratio becomes larger, a sudden drop of the values occurs.

This drop exists due to the activation of what is called a hump mode that is characterised by a decrease in the damping below zero followed by an increase. This activation is shown in Fig. 11. The curves on the left shows the apparition the hump but it remains positive and does not activate and then on the right, one of the parameters value has changed, forcing the hump to go below zero and the third mode to become the critical one.

With this jump from mode two to mode three, the flutter speed drops suddenly resulting in a sudden drop down of the flutter index. The dependency of the activation of the hump mode on
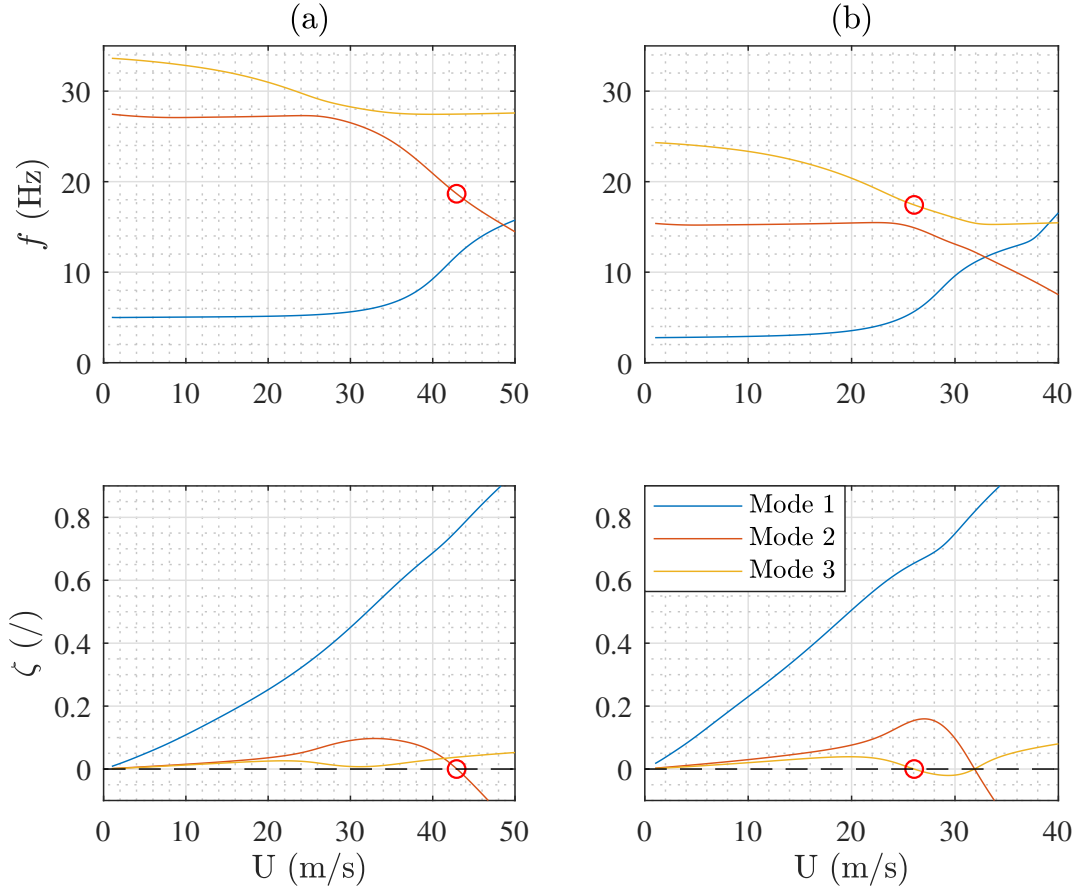
Figure 11: Comparison of the frquency and damping curves obtained for the three first eigenmodes for two different designs. (a) $AR = 3$, $\lambda = 0.5$ and $\Lambda = 0°$; (b) $AR = 4$, $\lambda = 0.5$ and $\Lambda = 0°$.

the parameters therefore needs deeper investigation before trying to fit any model. Note that the hump mode is unstable over a range of airspeeds only but it is directly followed by the classical hard flutter as shown in the figure that never stabilises. The critical flutter speed of the plate is therefore that of the hump mode activation.

2.4.2 Hump mode activation

To understand the discontinuity in the results, additional plates are modelled in the transition zone where the hump mode becomes active, for both $\Lambda = 0°$ and $\Lambda = 10°$. 27 plates are added to the initial domain which gives a total of $n = 91$ test cases on the basis of which the model is built. Use can be made of the results to try to deepen the understanding of the hump mode appearance and the reason of its activation. The classical bending-torsion flutter results from the complex coupling of the first torsion with bending. When the torsion corresponds to the second mode of the plate, the coupling is made with the first mode that corresponds to the first bending and the plate exhibits the classical flutter. Nevertheless, for all the plates that activate the hump mode (i.e. when the bump goes below the zero damping axis), the first three vibration modes are the first and second bending and the first torsion in ascending order of frequency. Note that for each mode, no perfect bending or torsion is obtained and they are always slightly mixed with a dominance of one or the other. In those cases, it is always the torsion mode that flutters. Other plates exhibit the appearance of the hump mode even if does not activate (as for plates 10 and 15) and for those, the torsion mode is again the third vibration mode. It is therefore the second bending mode that flutters in those cases. The hump mode appearance always comes with this specific order in the first threeeigenmodes. This could therefore be explained by a different coupling than the classical one of the torsion mode with the two bending modes whose frequencies are lower. As a consequence, the damping of the torsion mode would decrease until this special coupling stops making the damping increase again. Then, the classical bending torsion coupling takes place and the second bending mode damping decreases until the critical point and the wing flutters.

As shown, for some cases the hump mode is present and in addition to that the bump in the torsion mode damping curve crosses the zero axis making the mode flutters before the classical phenomenon takes place. The hump mode is thus active. Fig.12 depicts the variation of the frequency and damping curves of the first three modes for six different configurations. It appears that the hump mode becomes active when the difference between the wind-off natural frequencies corresponding to the third mode (first torsion) and the first one (first bending) decreases. The appearance of the hump could therefore result from the coupling between the first and third modes while its end would corresponds to the beginning of the coupling between the third and second mode. The activation would occur when the wind-off frequencies are close enough to each other strengthening the coupling that allows the bump to cross the zero axis.
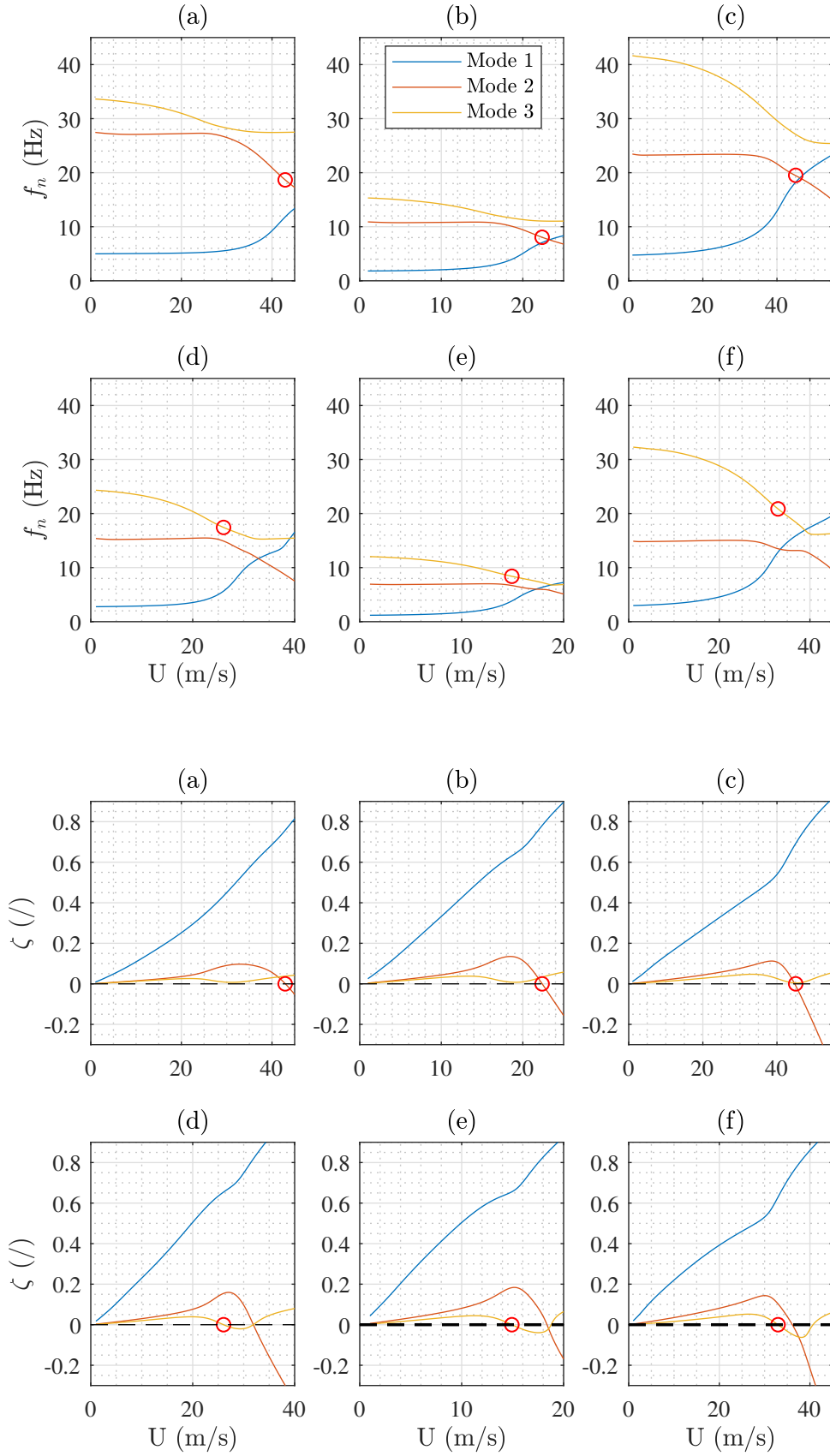
Figure 12: (a) $AR = 3$, $\lambda = 0.5$, $\Lambda = 0°$; (b) $AR = 4$, $\lambda = 0.75$, $\Lambda = 0°$; (c) $AR = 4$, $\lambda = 0.25$, $\Lambda = 10°$; (d) $AR = 4$, $\lambda = 0.5$, $\Lambda = 0°$; (e) $AR = 5$, $\lambda = 0.75$, $\Lambda = 0°$; (f) $AR = 5$, $\lambda = 0.25$, $\Lambda = 10°$.

Note that a possibility to get rid of the hump mode activation would be to increase the damping of the wing. The third mode damping curve would be translated upward and the bump would therefore not be able to cross the zero axis anymore.

With the flutter indices obtained, it appears that the two zones can be separated with a vertical plane as illustrated in Fig.13. The vertical planes delimiting the before and after hump activation
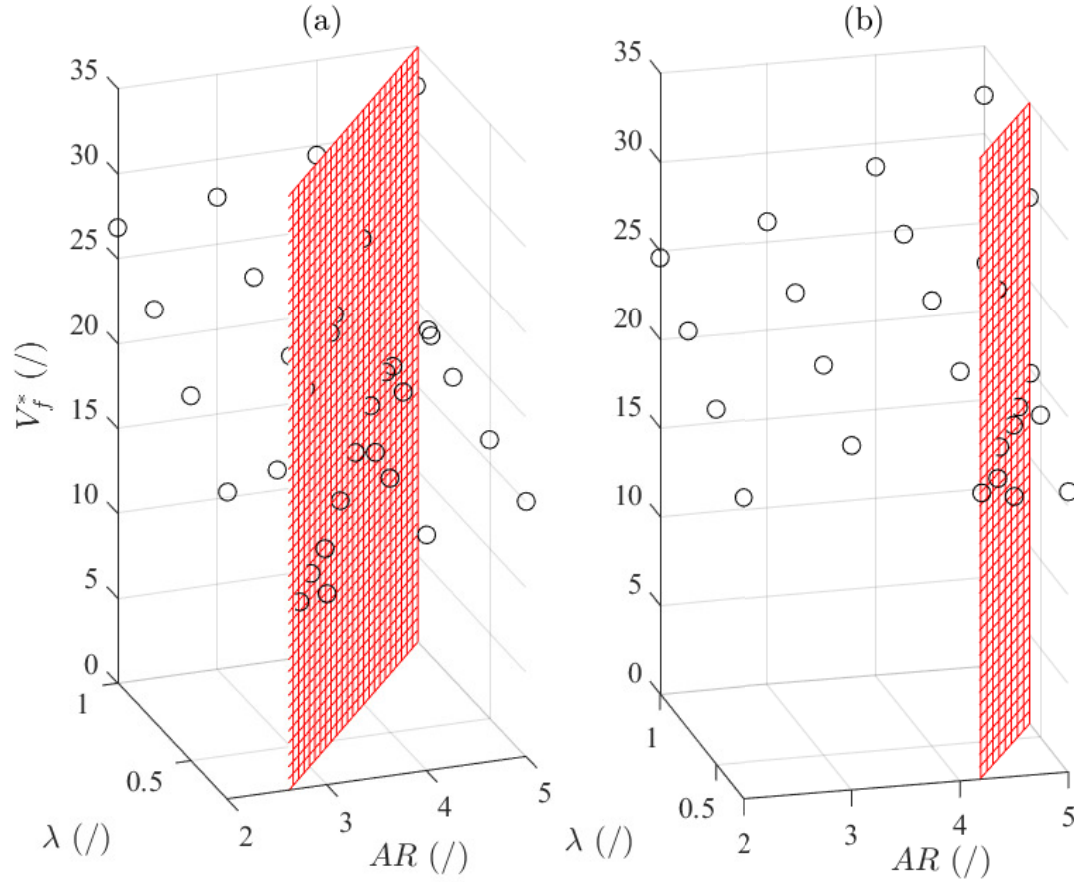
Figure 13: Illustration of the discontinuity plane in the results. (a) $\Lambda = 0°$; (b) $\Lambda = 10°$.

zones are generated with a first order equation in both cases in terms of the aspect and taper ratios

$$\begin{cases} \lambda = 0.31AR - 0.56 & \text{for} \quad \Lambda = 0° \\ \lambda = 0.42AR - 1.505 & \text{for} \quad \Lambda = 10° \end{cases} \tag{8}$$

To generalise those equations to any value of sweep angle, it is first assumed that both the slope and the intercept evolves linearly in terms of Λ so that if $\Lambda = 5°$,

$$m = \frac{0.31 + 0.42}{2} = 0.365 \qquad \text{and} \qquad p = \frac{0.56 + 1.505}{2} = 1.0325$$

giving the discontinuity equation

$$\lambda = 0.365AR - 1.0325 \tag{9}$$

To validate this equation, four more plates are modelled at the considered sweep angle and verification is made that the results are located in the expected zone. As shown in Tab.3, the cases for which the taper ratio is below the discontinuity line have undergone the transition of critical mode due to the hump mode activation. The assumption of linear evolution of the discontinuity line as a function of the sweep angle is then validated.

AR	λ	Λ	V_f^*	Hump activated
4	0.4	$\pi/36$	16.23	Yes
4	0.44	$\pi/36$	25.08	No
5	0.77	$\pi/36$	19.84	Yes
5	0.81	$\pi/36$	31.3	No

Table 3: Verification of the hump mode activation for $\Lambda = 5°$.

The equations of the variation of the slope and the intercept with the sweep angle can be obtained

$$m(\Lambda) = 0.63025\Lambda + 0.31 \qquad \text{and} \qquad p(\Lambda) = -5.41445\Lambda - 0.56 \tag{10}$$

and eventually, the general equation for the discontinuity line is given by

$$\lambda(AR, \Lambda) = (0.63025\Lambda + 0.31)AR - 5.41445\Lambda - 0.56 \tag{11}$$

The condition for the hump activation is to have a taper ratio below the discontinuity line.

The question that might come at this stage concerns the limit of the activation of the hump mode. Indeed, it has been shown in the previous section that when considering higher sweep angles, the discontinuity does not appear so that there must be a limit above which the phenomenon does not occur anymore on the design domain.

Looking at the variation of the discontinuity line, the last configuration of the design domain that should undergo hump activation is $AR = 5$ and $\lambda = 0.25$. Injecting those values in Eq.11, the hump activation is not expected to occur if $\Lambda > 0.327 \approx 18.73°$. However, it appears that for a configuration with $AR = 5$, $\lambda = 0.25$ and $\Lambda = 0.314 \approx 18°$, the critical mode is the second one
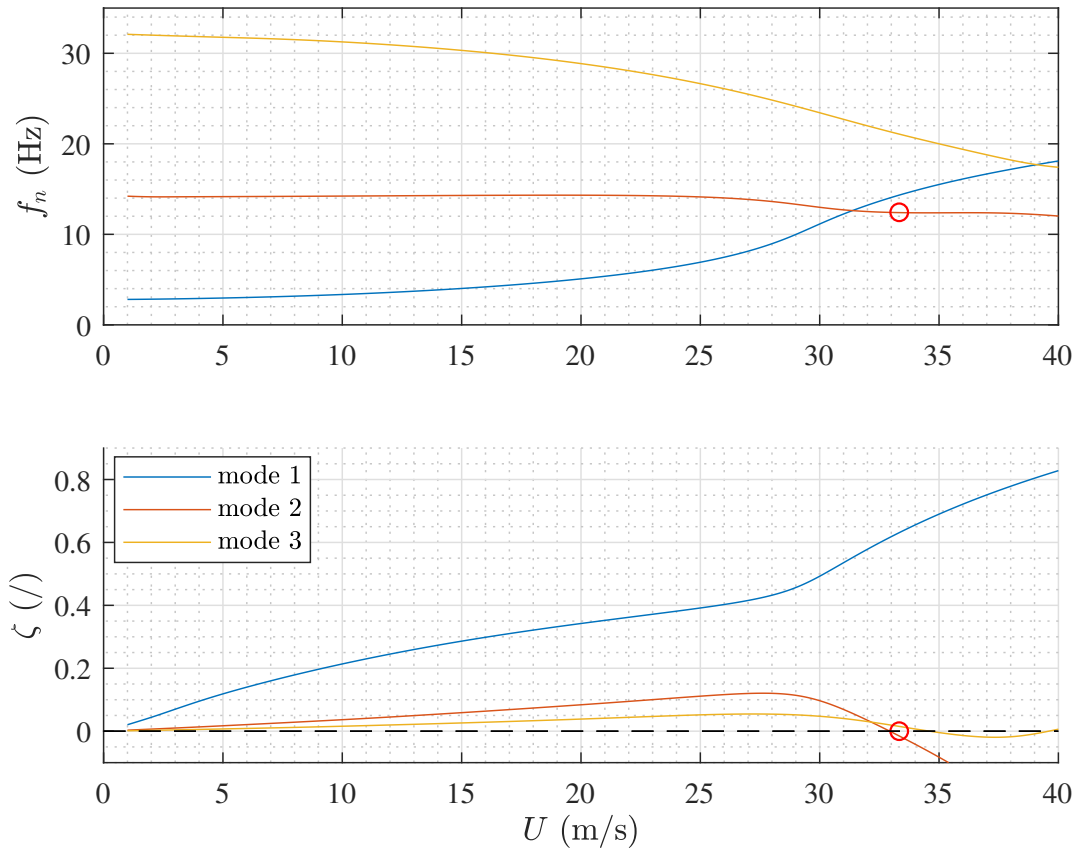
Figure 14: Frequency and damping curves obtained for the first three modes of configuration $AR = 5$, $\lambda = 0.25$ and $\Lambda = 18°$.

because the hump mode crosses the zero line for higher speeds as shown in Fig.14. Therefore, eventhough the hump mode is activated, it is not the critical one.

The first phenomenon that has been investigated consists in a vertical descent of the third mode damping curve until the hump crosses zero and becomes active which depends on the three variables but a second phenomenon takes place. With the sweep angle increasing, the damping curves of mode 2 and mode 3 moves horizontally with respect to each other so that their respective critical points end up switching their position making the second mode the critical one. This second phenomenon appears to be mostly depending on the sweep angle.

To illustrate this displacement of the curves with respect to each other and to assess its dependency on the three parameters, six configurations are compared and illustrated in Fig.15.
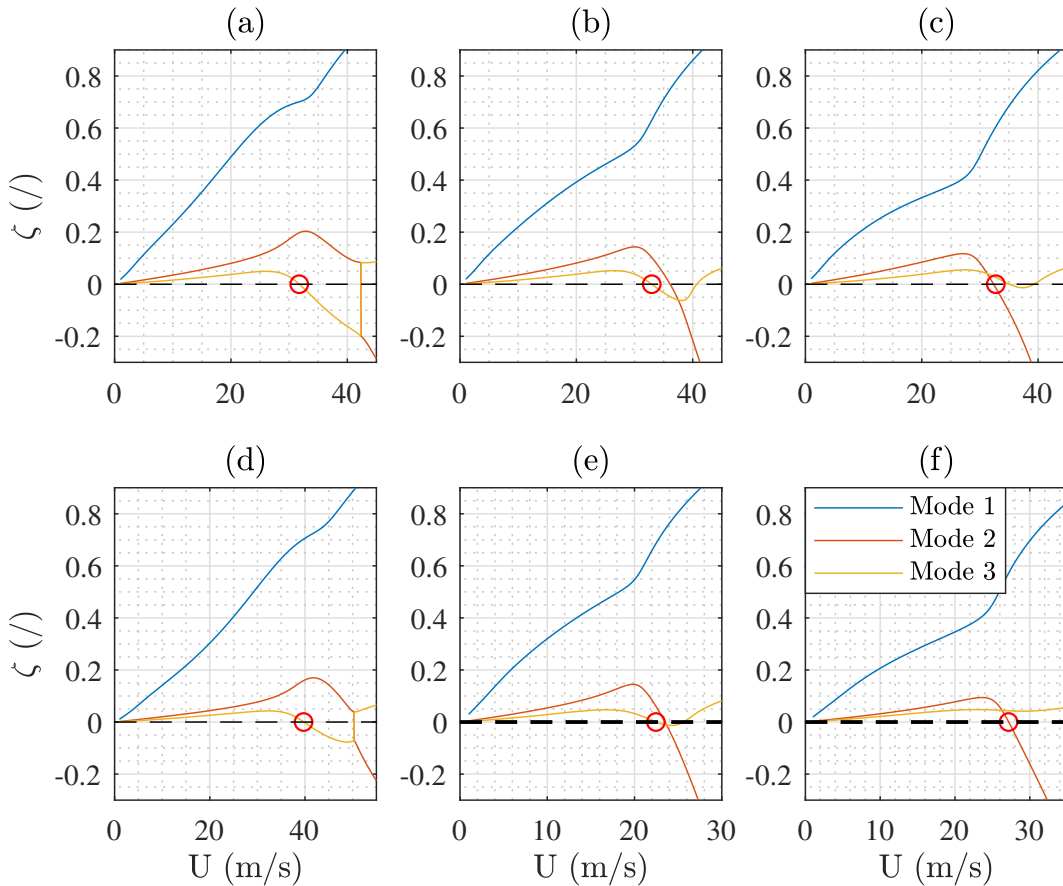
Figure 15: Damping curves obtained for the first three modes for configurations, (a) $AR = 5$, $\lambda = 0.25$, $\Lambda = 0°$; (b) $AR = 5$, $\lambda = 0.25$, $\Lambda = 10°$; (c) $AR = 5$, $\lambda = 0.25$, $\Lambda = 20°$; (d) $AR = 4$, $\lambda = 0.25$, $\Lambda = 0°$; (e) $AR = 5$, $\lambda = 0.5$, $\Lambda = 10°$; (f) $AR = 4$, $\lambda = 0.5$, $\Lambda = 20°$.

As expected from the discussion made above, the vertical displacement of the third mode curve depends on the three parameters. However, it appears clearly that the horizontal displacement of

the second and third modes curves with respect to each other is a phenomenon that is mainly sweep angle dependent. It is therefore assumed that only this parameters is responsible of the switch.

The sweep angle value for which the critical point switches from one mode to the other is obtained by plotting the curves of the critical speed obtained for both modes in Fig.16. Three configurations where hump is activated having the same aspect and taper ratios but different sweep angles are available. Two second order polynomials proposed in Eq.12 are used to fit the results for both modes and the residuals are respectively $1.2307 \cdot 10^{-14}$ and $7.1054 \cdot 10^{-15}$ for the second and third modes. As a consequence using higher order terms is not necessary and no additional configuration is required.

The two curves crosses each other for $\Lambda = 0.276 \approx 15.81°$ which corresponds to the flutter speed $V_\mathrm{f} = 34.14$ m/s.

$$
\begin{cases}
V_\mathrm{f} = 26.155\Lambda^2 - 36.668\Lambda + 42.27 & \text{for mode 2} \\
V_\mathrm{f} = 16.765\Lambda^2 + 4.1041\Lambda + 31.734 & \text{for mode 3}
\end{cases}
\tag{12}
$$

To summarise the discussion proposed, the hump mode is active up to $\Lambda = 0.327$. However, it remains the critical mode for flutter only up to $\Lambda = 0.276$ because for higher values, it is the second mode damping curve that crosses the zero axis for the lowest airspeed.

With the two phenomena limits being understood, the domain is divided into two distinct zones

- if $\Lambda < 0.276$ the hump mode is activated and is the critical mode if
  $\lambda(AR, \Lambda) < (0.63025\Lambda + 0.31)AR - 5.41445\Lambda - 0.56$.

- if $\Lambda \in [0.276; 0.327]$, the hump mode is active but it is not the critical flutter mode not matter the values selected for the aspect and taper ratios on the design domain considered here.

- if $\Lambda > 0.327$, the hump mode is never active and the second mode is the critical one.

2.4.3 Selection of the model

With the discontinuity being accurately defined, the model for the flutter index can be built. To this purpose, the linear regression theory is used in first place and the two zones of the domain are modelled separately. It must be reminded that the sweep angle Λ is taken in radians when building the models.
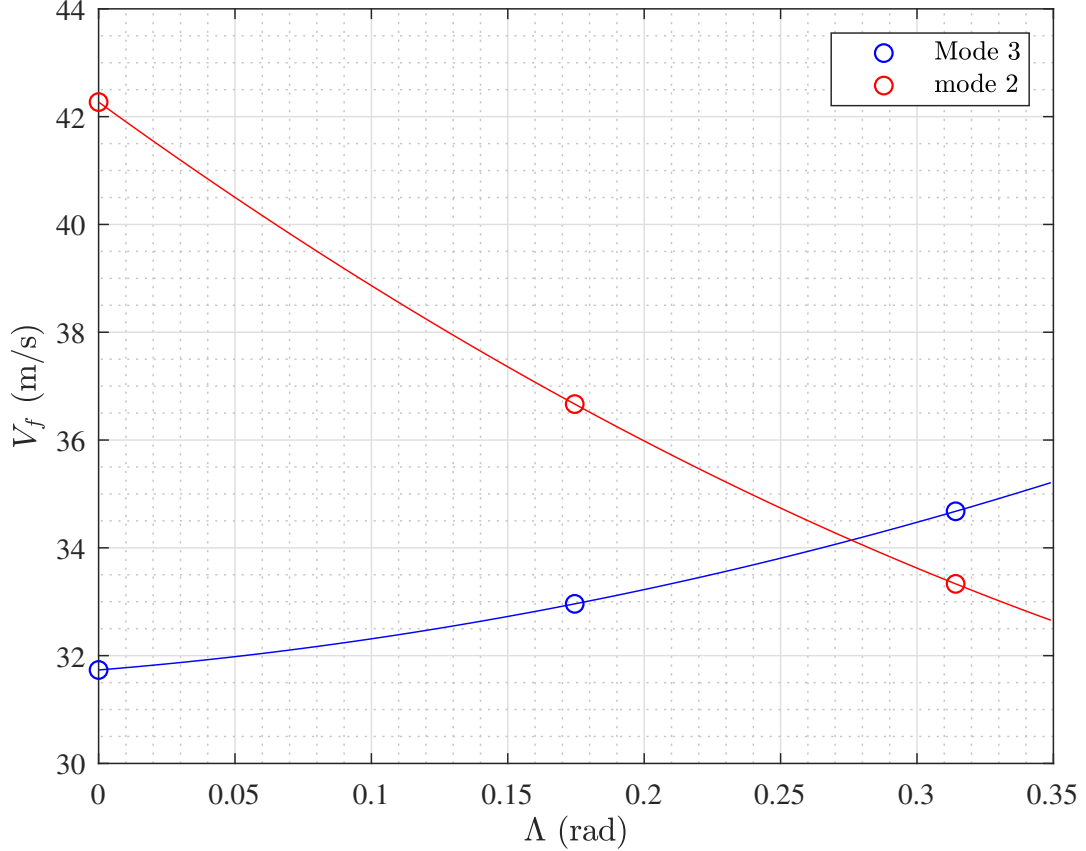
Figure 16: Variation of the critical flutter speeds for mode 2 and mode 3 as a function of the sweep angle. The three configurations have $AR = 5$ and $\lambda = 0.25$.

The general expression for any model is

$$Y(\mathbf{x}) = \hat{Y}(\mathbf{x}) + \varepsilon(\mathbf{x}) \tag{13}$$

where $Y(\mathbf{x})$ and $\hat{Y}(\mathbf{x})$ are respectively the observed and computed values depending on the factors contained in vector $\mathbf{x}$ and $\varepsilon(\mathbf{x})$ is the error term. In this context where no experiment has been used to build the model, no error can exist on the response or on the factor measurements and the error term is only the residual i.e. the difference between $Y(\mathbf{x})$ and $\hat{Y}(\mathbf{x})$ due to the lack of fit. Eq.13 can be written under the linear matrix form

$$\mathbf{Y}(\mathbf{x}) = \hat{\mathbf{Y}}(\mathbf{x}) + \boldsymbol{\varepsilon}(\mathbf{x}) = \mathbf{X}\boldsymbol{\beta} + \boldsymbol{\varepsilon}(\mathbf{x}) \tag{14}$$

where $\boldsymbol{\beta}$ is the vector of the model's parameters that must be computed, $\mathbf{X}$ is the model's matrix and the product $\mathbf{X}\boldsymbol{\beta}$ is the expectation function. The linearity is in term of the model parameters meaning that the derivative of $\mathbf{Y}(\mathbf{x})$ with respect to $\boldsymbol{\beta}$ is independent of $\boldsymbol{\beta}$.

First order polynomial

The first and most simple model that can be used is the first order polynomial given by

$$\hat{Y}(\mathbf{x}) = \beta_0 + \sum_{i=1}^{m} \beta_i x_i \tag{15}$$

where

- β_0 represents the mean effect i.e. the intercept of the model

- β_i represents the linear effect of the ith factor

and the number of parameters that must be computed is $p = 4$. Using the matrix form of Eq.14, the model's matrix is built as

$$\mathbf{X} = \begin{bmatrix} 1 & AR_1 & \lambda_1 & \Lambda_1 \\ 1 & AR_2 & \lambda_2 & \Lambda_2 \\ \vdots & \vdots & \vdots & \vdots \\ 1 & AR_n & \lambda_n & \Lambda_n \end{bmatrix} \qquad (n \times p) \tag{16}$$

with the first column is made of 1's that multiply the mean effect β_0. To find the parameters values, use is make of the least square estimates which provides the estimators $\hat{\boldsymbol{\beta}}$ according to

$$\hat{\boldsymbol{\beta}} = (\mathbf{X}^{\mathrm{T}}\mathbf{X})^{-1}\mathbf{X}^{\mathrm{T}}\mathbf{Y} \tag{17}$$

In a classical statistical context, the use of least squares estimates requires to verify several assumptions to produce the best possible estimates. Those assumptions mainly concern the error term but here, they are only made of the residuals existing between the response and the expectation function so that they can not be analysed as classical experimental errors.

Nevertheless, as shown in Eq.17, it is required to compute the inverse of $\mathbf{X}^{\mathrm{T}}\mathbf{X}$ which imposes that the matrix in not singular. To avoid the singularity problem, the model's matrix should be of full rank so that the computation of the estimators is possible and accurate.

As mentioned previously the two zones of the domain must be modelled separately. Using Eq.17 in both cases, the model's parameters are obtained and the first order model is written under the conditional form

- if $\Lambda \in \begin{bmatrix} 0 \; ; \; 0.276 \end{bmatrix}$

▹ if $\lambda < (0.63025\Lambda + 0.31)AR - 5.41445\Lambda - 0.56$, the hump mode is the critical one and

$$\hat{V}_\mathrm{f}^* = 4.4228 + 1.6895 \cdot AR + 7.224 \cdot \lambda + 13.036 \cdot \Lambda \tag{18}$$

▹ else, the hump mode is not activated and

$$\hat{V}_\mathrm{f}^* = 9.4001 + 3.0199 \cdot AR + 8.7992 \cdot \lambda - 1.7893 \cdot \Lambda \tag{19}$$

• if $\Lambda > 0.276$, the critical points have switched their locations so that the hump mode is not the critical one and Eq.19 is to be used.

Fig.17 presents the results obtained with the first order model under the form of surfaces for each value of sweep angle. The independent variables being taken alone in the model, curvature in the
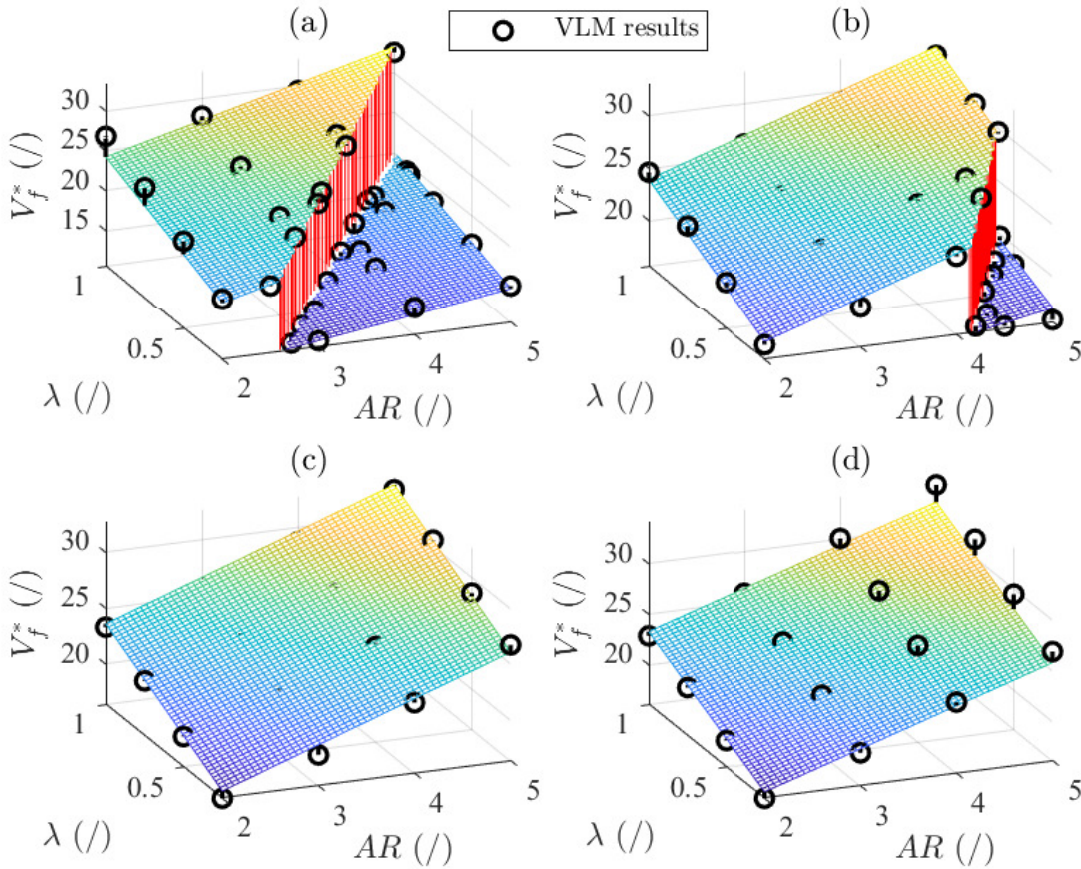
Figure 17: First order model without interaction term. (a) $\Lambda = 0°$; (b) $\Lambda = 10°$; (c) $\Lambda = 20°$; (d) $\Lambda = 30°$.

surfaces can not exist which limits the possibility to get close to each of the VLM results. With this first order polynomial, the maximum residual obtained where the hump mode is not active

is $\varepsilon_{\text{no hump}} = 2.59$ while for the zone where the activation took place, it is $\varepsilon_{\text{hump}} = 0.904$ which correspond respectively to 9.66% and 6.51% of the corresponding observed response.

Second order polynomial without direct terms

To enhance the quality of the results, some curvature can be brought by adding 2nd order terms through the interaction between the factors. The second order with interaction terms polynomial takes the general form

$$\hat{Y}(\mathbf{x}) = \beta_0 + \sum_{i=1}^{m} \beta_i x_i + \sum_{i \, < \, j} \sum \beta_{ij} x_i x_j \tag{20}$$

where β_{ij} represents the interaction effect between factors i and j.

The total number of parameters to be estimated is $p = 7$ and the model's matrix is constructed as

$$\mathbf{X} = \begin{bmatrix} 1 & AR_1 & \lambda_1 & \Lambda_1 & AR_1 \cdot \lambda_1 & AR_1 \cdot \Lambda_1 & \lambda_1 \cdot \Lambda_1 \\ 1 & AR_2 & \lambda_2 & \Lambda_2 & AR_2 \cdot \lambda_2 & AR_2 \cdot \Lambda_2 & \lambda_2 \cdot \Lambda_2 \\ \vdots & \vdots & \vdots & \vdots & \vdots & \vdots & \vdots \\ 1 & AR_n & \lambda_n & \Lambda_n & AR_n \cdot \lambda_n & AR_n \cdot \Lambda_n & \lambda_n \cdot \Lambda_n \end{bmatrix} \tag{21}$$

The model's parameters estimators are again obtained using the least square estimates and the model takes the form

- if $\Lambda \in \left[0 \; ; \; 0.276 \right]$

  ▷ if $\lambda < (0.63025\Lambda + 0.31)AR - 5.41445\Lambda - 0.56$

$$\hat{V}_{\text{f}}^* = -0.5328 + 2.8805 \cdot AR + 18.0192 \cdot \lambda + 71.4015 \cdot \Lambda$$
$$-2.4927 \cdot AR \cdot \lambda - 15.45 \cdot AR \cdot \Lambda + 32.6467 \cdot \lambda \cdot \Lambda \tag{22}$$

  ▷ else

$$\hat{V}_{\text{f}}^* = 10.7734 + 2.4343 \cdot AR + 11.0768 \cdot \lambda - 10.4523 \cdot \Lambda$$
$$-0.4436 \cdot AR \cdot \lambda + 2.965 \cdot AR \cdot \Lambda - 1.8488 \cdot \lambda \cdot \Lambda \tag{23}$$

- if $\Lambda > 0.276$, Eq.23 is to be used.

whose results are shown in Fig.18.

With this model comprising the interaction terms, the maximum residuals become $\varepsilon_{\text{no hump}} = 1.008$ and $\varepsilon_{\text{hump}} = 0.889$ which represents respectively 4.15% and 6.4% of the corresponding VLM
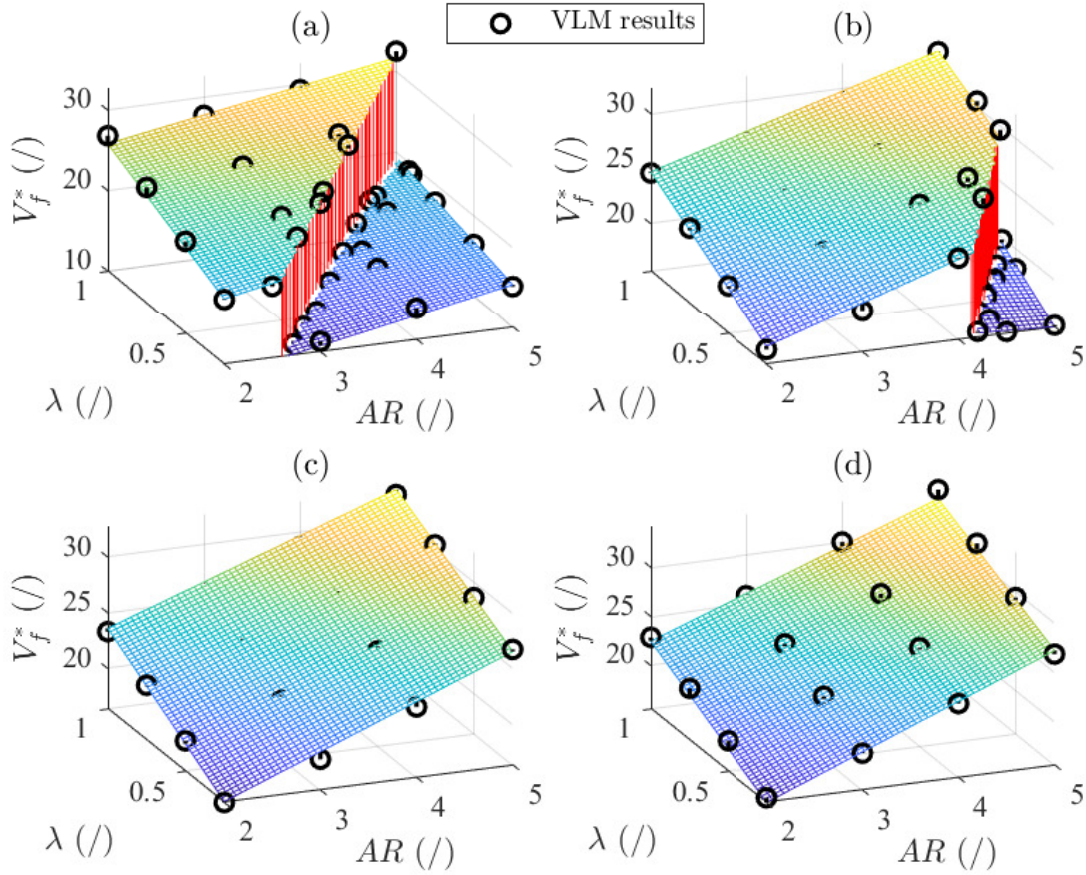
Figure 18: Second order polynomial without direct terms. (a) $\Lambda = 0°$; (b) $\Lambda = 10°$; (c) $\Lambda = 20°$; (d) $\Lambda = 30°$.

results which shows that the added terms have significantly improved the quality of the model for the zone where the hump is not active. For the hump-activated zone, maximum residual has been decreased from 0.11% only. Note that the maximum residuals are not obtained for the same VLM results for each tested model.

Complete second order polynomial

The two models presented above are often lacking of accuracy because no direct quadratic term exists to create curvature where it is required. To overcome this problem, a solution is to use a complete second order polynomial that has higher flexibility to adapt to the observed response points since it can take a lot of functional forms. Some of them are presented in Fig.19.
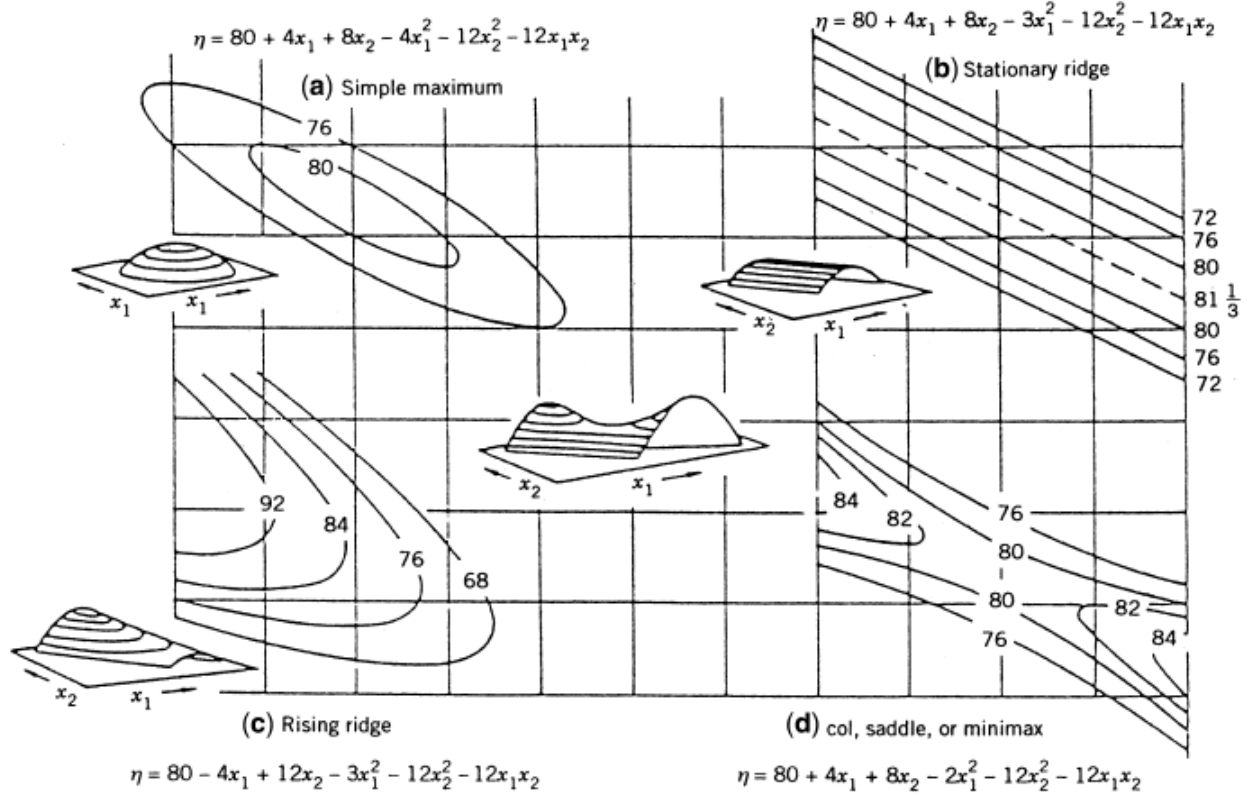
Figure 19: Examples of functional forms defined by second order models, taken from [6].

A complete second order model takes the general form

$$\hat{Y}(\mathbf{x}) = \beta_0 + \sum_{i=1}^{m} \beta_i x_i + \sum_{i=1}^{m} \beta_{ii} x_i^2 + \sum_{i \,<\, j} \sum \beta_{ij} x_i x_j \tag{24}$$

where β_{ii} represents the quadratic effect of the ith factor.

The total number of parameters to be estimated is $p = 10$ and the model's matrix takes the form

$$\mathbf{X} = \begin{bmatrix} 1 & AR_1 & \lambda_1 & \Lambda_1 & AR_1^2 & \lambda_1^2 & \Lambda_1^2 & AR_1 \cdot \lambda_1 & AR_1 \cdot \Lambda_1 & \lambda_1 \cdot \Lambda_1 \\ 1 & AR_2 & \lambda_2 & \Lambda_2 & AR_2^2 & \lambda_2^2 & \Lambda_2^2 & AR_2 \cdot \lambda_2 & AR_2 \cdot \Lambda_2 & \lambda_2 \cdot \Lambda_2 \\ \vdots & \vdots & \vdots & \vdots & \vdots & \vdots & \vdots & \vdots & \vdots & \vdots \\ 1 & AR_n & \lambda_n & \Lambda_n & AR_n^2 & \lambda_n^2 & \Lambda_n^2 & AR_n \cdot \lambda_n & AR_n \cdot \Lambda_n & \lambda_n \cdot \Lambda_n \end{bmatrix} \tag{25}$$

With this model, the problem of having the model's matrix that is not of full rank appears. Indeed, when adding the direct quadratic terms, collinearity occurs which reduces the rank of the matrix and this trouble takes place when modelling the zone after the hump activation. A complete second order polynomial can therefore not be used in this zone.

- **Incomplete second order polynomial**

A way of improving the quality of the results and overcoming the problem of collinearity is to start with the second order model with the interaction terms only and try to add second order terms as long as the model's matrix remain of full rank which is called forward selection. In fact, the trouble arises when adding the Λ^2 term. Consequently, the incomplete second order polynomial model with a full rank model's matrix is the same as for the complete second order one with the Λ^2 term removed. The total number of model's parameters is therefore $p = 9$ and the model's matrix is given by

$$\mathbf{X} = \begin{bmatrix} 1 & AR_1 & \lambda_1 & \Lambda_1 & AR_1^2 & \lambda_1^2 & AR_1 \cdot \lambda_1 & AR_1 \cdot \Lambda_1 & \lambda_1 \cdot \Lambda_1 \\ 1 & AR_2 & \lambda_2 & \Lambda_2 & AR_2^2 & \lambda_2^2 & AR_2 \cdot \lambda_2 & AR_2 \cdot \Lambda_2 & \lambda_2 \cdot \Lambda_2 \\ \vdots & \vdots & \vdots & \vdots & \vdots & \vdots & \vdots & \vdots & \vdots & \vdots \\ 1 & AR_n & \lambda_n & \Lambda_n & AR_n^2 & \lambda_n^2 & AR_n \cdot \lambda_n & AR_n \cdot \Lambda_n & \lambda_n \cdot \Lambda_n \end{bmatrix} \tag{26}$$

The zone where the hump mode is not active is modelled with a complete second order polynomial while the hump-activated zone is modelled with an incomplete second order one. The model takes the form

- if $\Lambda \in \begin{bmatrix} 0 \; ; \; 0.276 \end{bmatrix}$

  ▹ if $\lambda < (0.63025\Lambda + 0.31)AR - 5.41445\Lambda - 0.56$

$$\hat{V}_{\mathrm{f}}^* = -9.1804 + 8.7093 \cdot AR + 7.3569 \cdot \lambda + 38.5296 \cdot \Lambda$$
$$-0.7797 \cdot AR^2 + 5.1404 \cdot \lambda^2 \tag{27}$$
$$-1.4957 \cdot AR \cdot \lambda - 9.2776 \cdot AR \cdot \Lambda + 42.3495 \cdot \lambda \cdot \Lambda$$

  ▹ else

$$\hat{V}_{\mathrm{f}}^* = 13.1303 + 0.4705 \cdot AR + 14.4587 \cdot \lambda - 14.8645 \cdot \Lambda$$
$$+0.3275 \cdot AR^2 - 2.4899 \cdot \lambda^2 + 10.3014 \cdot \Lambda^2 \tag{28}$$
$$-0.6197 \cdot AR \cdot \lambda + 2.4378 \cdot AR \cdot \Lambda - 1.0534 \cdot \lambda \cdot \Lambda$$

- if $\Lambda > 0.276$, Eq.28 is to be used.

With this second order model whose results are shown in Fig.20, the maximum residuals are $\varepsilon_{\text{no hump}} = 0.72$ and $\varepsilon_{\text{hump}} = 0.502$ which represents respectively 2.69% and 2.9% of the corresponding VLM results. Again, the quality of the results in the zone before the hump activation has been significantly improved. Moreover, it appears that the addition of the direct quadratic terms have improved a lot more significantly the fit in the zone after the hump activation in comparison to the model comprising the interaction terms only. A decrease of the maximum residual of 3.5% is observed.
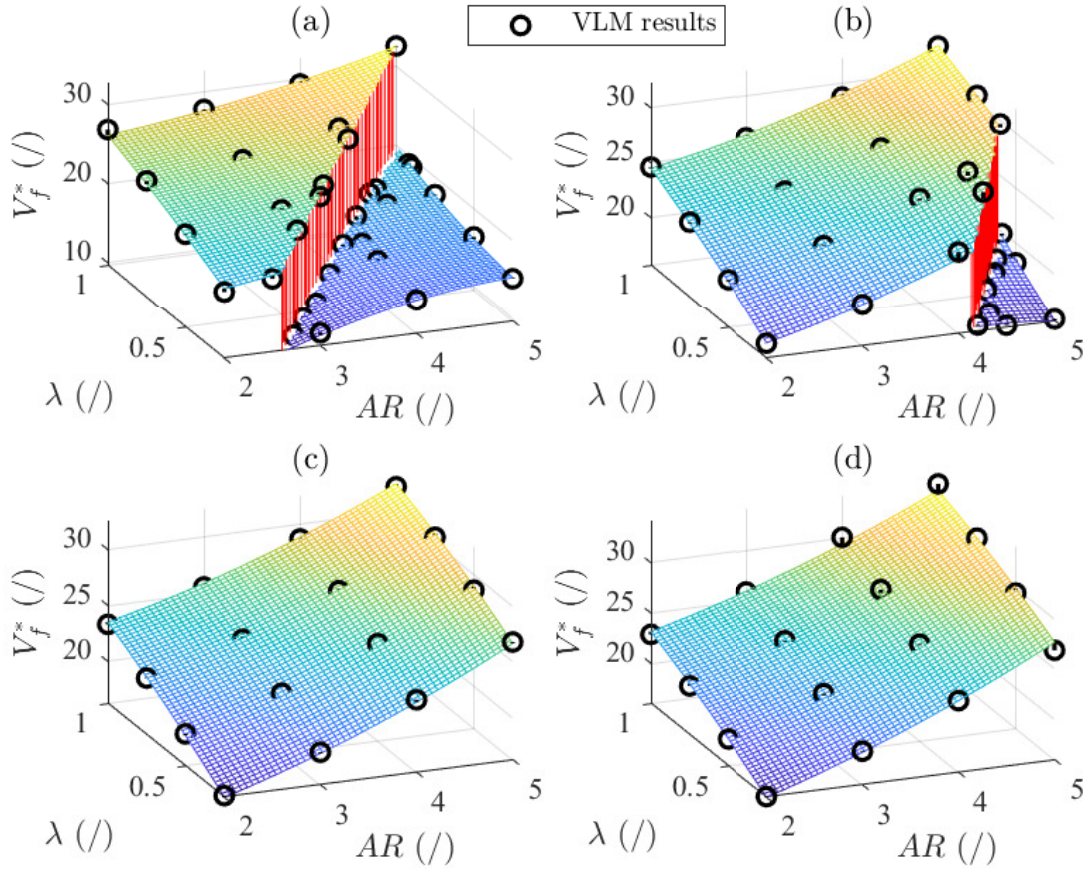
Figure 20: Complete second order model for the zone before the discontinuity and incomplete second order model for the zone after the discontinuity. (a) $\Lambda = 0°$; (b) $\Lambda = 10°$; (c) $\Lambda = 20°$; (d) $\Lambda = 30°$.

Comparison of the models

As the problem of collinearity appeared in the second order model's matrix, trying to fit a higher order polynomials brings the risk of suffering from singularity problem in Eq.17 computing the estimators for the model's parameters. Additionally, the computation of the flutter indices could become much heavier when adding higher order terms without improving the results significantly. Therefore, It has been decided to compare the three models described above for the linear regression theory before potentially trying to fit a nonlinear prediction law on the results if necessary.

Two methods for comparing the models are used

- comparison of the maximum residual:
  the maximum residuals as well as their percentages relative to the corresponding responses have been given for each model type and for the two zones of the domain. For the first order model, the maximum error for the zone where the hump is not active goes up to almost 10% of the response which is due to the absence of curvature. This types of model is mainly used when there are a lot of independent variables that might have an impact on the response to determine which ones are the most important to take into account (screening experiment). In this context, the factors have been selected at the very beginning knowing that each one of them is of prior importance in the flutter phenomenon and the others have been fixed for all the tests. It was expected that a first order model could not represent perfectly the phenomenon.
  Going from a second order model with the interaction terms only to the second order model containing direct terms allows to reduce the maximum residuals of 35% and 55% respectively for the before and after hump activation zones which shows that the direct quadratic terms enhance significantly the quality of the results and especially on the area where the hump mode is active. Nevertheless, it must be noticed that the maximum residuals are not obtained at the same location for the three model's types.
  In the end, from the residuals point of view, selecting a model constructed with the second order polynomials is the best choice. It provides the most accurate results with an error that remains below 3% of the observed flutter index.

- Multiple linear correlation coefficient:
  the quality of the model can be assessed more generally by computing the sum of the mean

squared error obtained for each observed value. Following the definition proposed in [7], the mean squared error is given by

$$MSE = \frac{SSE}{n-p} = \frac{\sum_{i=1}^{n}(Y_i - \hat{Y}_i)^2}{n-p} \tag{29}$$

where SSE is the Sum of the Squares of the Errors and $n - p$ corresponds to the number of degree of freedom. The total number of test cases are reespectively $n = 64$ and $n = 27$ for the zones before and after the hump activation.

Again, the two zones of the domain are treated separately and the SSE and MSE values are given for each model in Tab.4

	1$^{\text{st}}$ order		2$^{\text{st}}$ order with interaction only		2$^{\text{nd}}$ order	
	SSE (/)	MSE (/)	SSE (/)	MSE (/)	SSE (/)	MSE (/)
Inactive hump mode	40.85	0.68	17.655	0.31	5.4	0.1
Active hump mode	7.03	0.306	2.6	0.13	1.03	0.057

Table 4: SSE and MSE values for the two zones of the three models.

The best model is the one that minimises the MSE i.e., the difference between the fitted and the observed results. As for the analysis of the maximum residuals, the 2$^{\text{nd}}$ order model is the one providing the most accurate results. However, some criterion is required to be able to make a selection that should result from a trade off between accuracy and complexity of the model and a threshold value needs to be selected.

To this purpose, the multiple linear correlation coefficient is defined

$$R^2 = 1 - \frac{SSE}{SST} = 1 - \frac{SSE}{\sum_{i=1}^{n}(Y_i - \bar{Y})^2} \tag{30}$$

with SST the Sum of the Squares Total and the closer R^2 gets to 1, the better the model. For the three models, the correlation coefficients are provided in Tab.5 and they all provide results that are generally very accurate.

	1st order	2st order with interaction only	2nd order
Inactive hump mode	0.9644 (/)	0.9846 (/)	0.9953 (/)
Active hump mode	0.9569 (/)	0.9841 (/)	0.9937 (/)

Table 5: Multiple linear correlation coefficients R^2 for the two zones of the three models.

From the correlation coefficient point of view, the three models provide highly reliable results. However, it is to be noted that the correlation coefficient is a general value computed for the whole set of data points. As a consequence, having a large number of data could attenuate too much the few results that are badly modelled despite their importance in the modelling process. The analysis of the maximum residual has therefore to be used to ensure that all the points are modelled separately with enough accuracy.

On the one hand, the first order model has a maximum error of 10% of the observed value due to the absence of curvature so that this model can not be selected. On the other hand, the second order model with the direct terms is the one providing the most accurate results from both a local and a general points of view. However, all the terms are probably not bringing a significant amount of information to the model and the discussion about which terms must be retained is made in the following section.

2.4.4 Backward elimination

In the previous section, the second order model has been obtained by adding direct second order terms so that the model's matrix remains of full rank. Starting from this polynomial, a backward elimination can be done to remove the terms that do not bring useful information in the model. In this analysis, given that the second order model ensures up to 99.53% and 99.37% of accuracy respectively for the before and after hump activation zones, it has been decided to not go below 99% for the two zones. Also, the maximum allowed residual is set to be 3.5% of the observed response.

To determine which terms can be removed, use is made of the model's parameters given that the importance of each term in the model is illustrated by the value of the coefficient. However, the domain has not been normalised so that a direct comparison can not be made and each coefficient has

to be multiplied by the maximum value of the independent variable it multiplies. The elimination is then achieved step by step, removing the terms having the smallest normalised coefficient and assessing the quality of the model using the multiple linear correlation coefficient and the maximum residuals.

In the end,

- for the zone where the hump mode is inactive, the 2nd, 6th and 10th terms corresponding respectively to AR, λ^2 and $\lambda \cdot \Lambda$ can be removed. The correlation coefficient is equal to $R^2 = 0.9936$ and the maximum residual corresponds to 2.17% of the response.

- For the zone where the hump mode has been activated, the 6th and 7th terms, corresponding respectively to λ^2 and $AR \cdot \lambda$ can be removed. The correlation coefficient is equal to $R^2 = 0.9914$ and the maximum residual corresponds to 3.2% of the response.

2.4.5 Final model

With the comparison being made between the models and the elimination of the useless terms, the final model characterising the flutter index of flat cantilever plates of thickness 1 mm and root chord 200 mm is obtained as an incomplete second order polynomial

- if $\Lambda \in \left[0 \; ; \; 0.276 \right]$

  ▸ if $\lambda < (0.63025\Lambda + 0.31)AR - 5.41445\Lambda - 0.56$

$$\hat{V}_{\text{f}}^* = -9.6713 + 9.0035 \cdot AR + 6.1663 \cdot \lambda + 35.4463 \cdot \Lambda - 0.8803 \cdot AR^2$$
$$-7.7487 \cdot AR \cdot \Lambda + 30.3958 \cdot \lambda \cdot \Lambda \tag{31}$$

  ▸ else

$$\hat{V}_{\text{f}}^* = 14.8434 + 11.1095 \cdot \lambda - 15.6228 \cdot \Lambda + 0.4039 \cdot AR^2 + 10.7252 \cdot \Lambda^2$$
$$-0.6591 \cdot AR \cdot \lambda + 2.356 \cdot AR \cdot \Lambda \tag{32}$$

- if $\Lambda > 0.276$, Eq.32 is to be used.

whose results are illustrated in Fig.21.
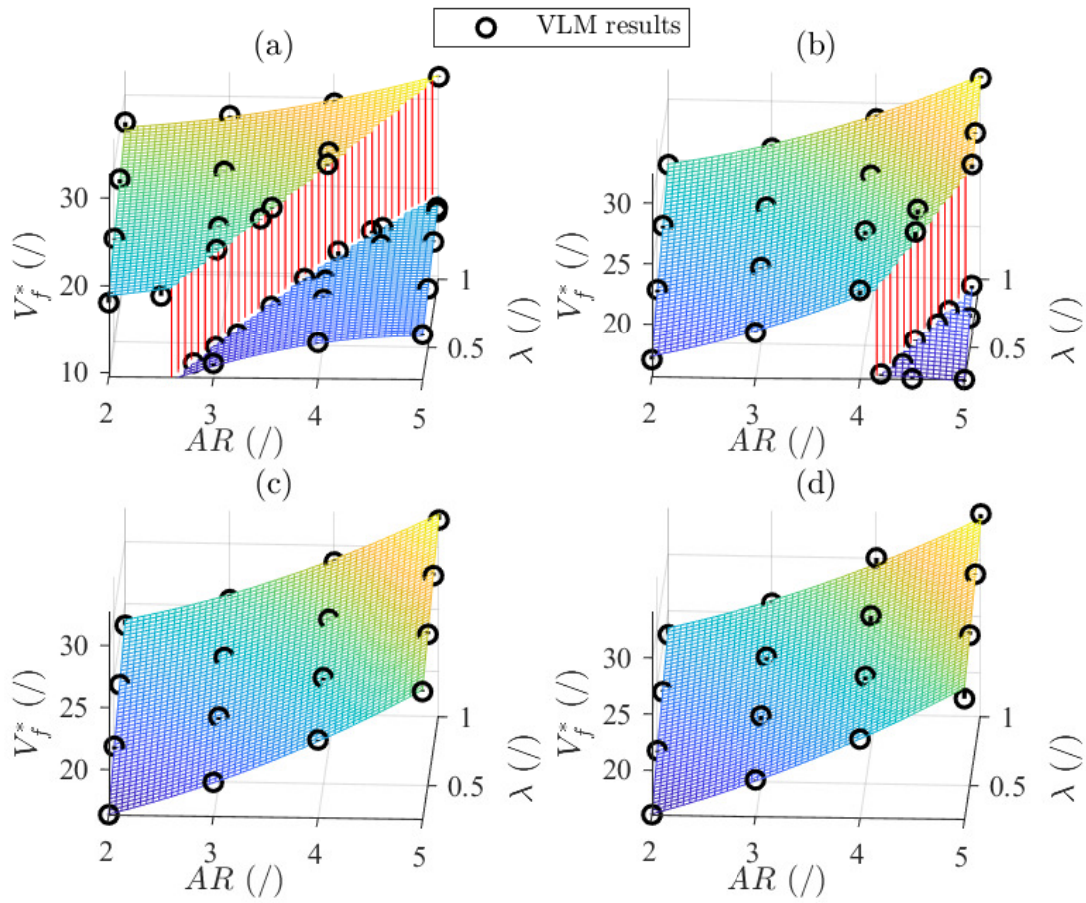
Figure 21: Final model. (a) $\Lambda = 0$; (b) $\Lambda = \pi/18$; (c) $\Lambda = \pi/9$; (d) $\Lambda = \pi/6$.

With this final model consisting in two different incomplete second order polynomials for the two zones of the domain, the maximum residuals are 2.17% and 3.22% respectively for the zone before and after the hump activation. The multiple correlation coefficients for those two zones are respectively equal to $R^2 = 0.9936$ and $R^2 = 0.9914$ so that on the basis of the numerical results, the model is highly reliable.

3 Experimental comparison

At the beginning of this work it was expected to perform practical experiments at the wind tunnel of the UNIVERSITY OF LIEGE to validate the model presented in the previous section. To this purpose an excitation system has been designed and several plates were expected to be tested. However, the sanitary crisis of the Covid-19 prevented most of the experimental tests from being carried out. Consequently, only two plates have been tested. Also, the tests had to be performed within a short period of time which prevented them to be conducted as accurately as it should have been.

The following is therefore dedicated to the discussion about the experimental tests and the comparison of their results with the model constructed previously.

3.1 Excitation system

The flutter phenomenon consists in an amplification of the motion's amplitude when the critical speed has been reached. Therefore, the plates are expected to be tested at different airspeeds until flutter is reached. To do so, use is make of an excitation system on which the plate is fixed at its root. This system allows to properly identify the vibration modes whose frequencies vary with the airspeed despite the increase of the damping due to the airflow at subcritical speeds. It has been designed for this master thesis and assembled by V2I Company located in the Science Park of Liège.

The system is expected to be fixed on the turning table of the wind tunnel so that a circular fixation plate supports the whole device. The excitation is delivered by a shaker whose reference is TV 51075-M Vibration Test System, from the TIRA Company, that is linked to a mobile cart through a connecting rod. This cart is made of four linear bearings that slide on fixed steel shafts. The whole system is covered by a large circular plate acting as an end plate to avoid interference between the airflow coming onto the excitation system and that coming onto the tested plate. Finally, to fix the plate on the system and reproduce a clamping boundary condition, a squeezing plate of 5cm high is pressed against the upper part of the cart with the wing in between and four screws are used for tightening.

All the components are made of aluminium except the shafts and their supports that are made of steel.

It is expected that the eigenmodes of the system do not interfere with the measurements so that

the dimensions and the materials have been selected, with a certain amount of safety, in adequacy with the range of frequencies that were of interest for observing flutter. Again, the modal analysis has been achieved with NX Nastran and the first three eigenmodes of the system as well as its design are illustrated in Tab.6. The blue part of the first drawing shows the cart i.e. the moving part of the system while the green one corresponds to the shaker.

	mode 1, f_1 = 117.87 Hz
mode 3, f_2 = 134.28 Hz	mode 4, f_3 = 141.04 Hz
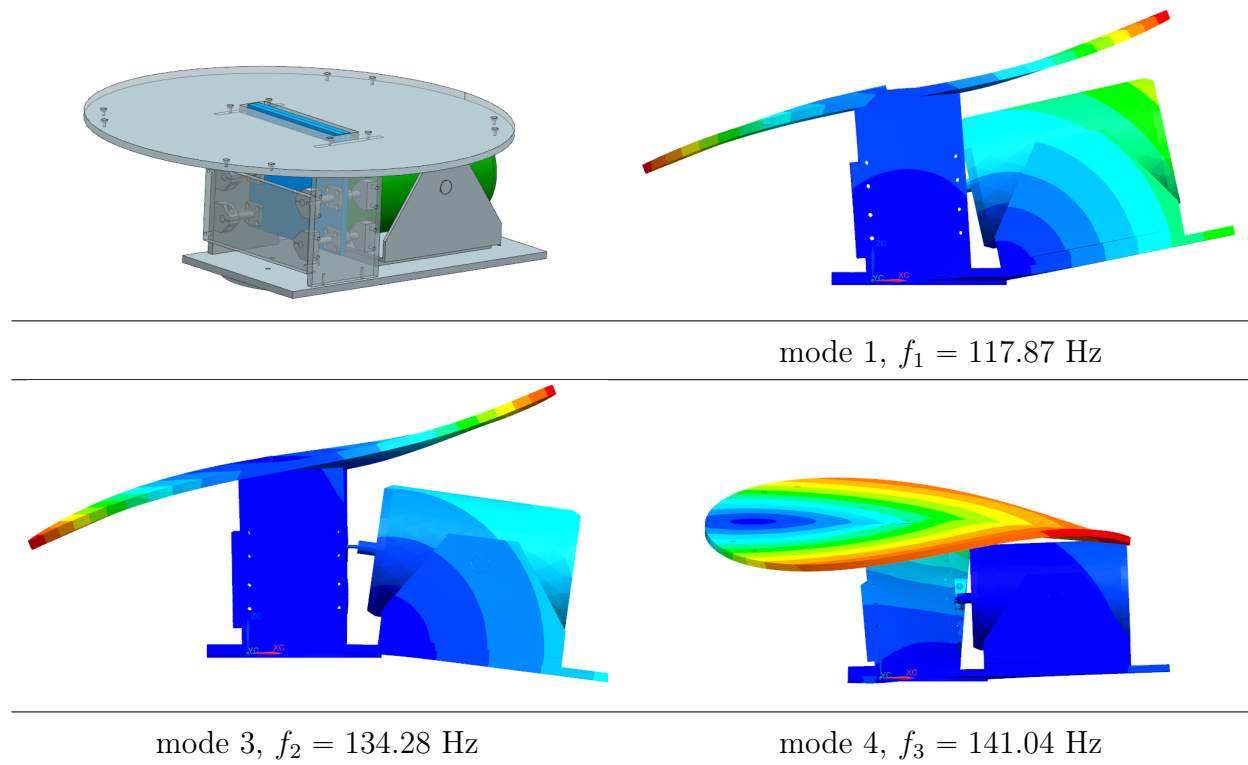
Table 6: Illustration and modal analysis of the excitation system.

Four measurement devices are used. A load cell located on the rod connecting the cart and the shaker measures the force that is delivered by the shaker which is the input signal used to compute the Frequency Response Functions (FRF's). At the same location, an accelerometer measures the acceleration of the cart. The displacments of the plates are measured using two lasers having a range of 0.5m. The distance is measured with the light that is reflected on the plates and pieces of tapes are used to reduce the diffusivity of the reflection due to the aluminium. The noise existing in the signals is therefore reduced. Also, The shaker being connected to the ground of the wind tunnel, the support of the lasers is fixed to ceiling to avoid any transmission of the vibrations through the ground.

Finally, bending and torsion are expected to be captured correctly. To this purpose, the two lasers are not located on the same horizontal or vertical lines. One is pointing near the leading edge and near the tip chord while the other one is pointing near the trailing edge and closer to the root

chord. In this configuration, subtracting the two signals should highlight the torsion mode and higher order bending modes. The complete setup is illustrated in Fig.22 with a rectangular plate.

Figure 22: Experimental setup used for the wind tunnel experiments.

3.2   Experimental modal analysis

The signals obtained during the tests in the temporal domain are converted in the frequency domain through the use of the Fourier transform and the FRF's are computed using the force signal that corresponds to the input one. Then to extract the useful information from those data, use is made of the Polyreference Least Squares Complex Frequency (Polymax) method described in [10] and the MATLAB code has been written by Prof. G. Dimitriadis. The poles of the FRF's are obtained on the basis of a so-called right matrix-fraction model.

The rows of the right matrix-fraction model are written as

$$\langle \hat{H}(\omega) \rangle = \langle B(\omega) \rangle \left[A(\omega) \right]^{-1} \tag{33}$$

where

$$\langle B(\omega) \rangle = \sum_{r=0}^{p} \Omega_r(\omega) \langle \beta_r \rangle \qquad \text{and} \qquad [A(\omega)] = \sum_{r=0}^{p} \Omega_r(\omega) [\alpha_r] \tag{34}$$

with $\Omega_r(\omega)$ the polynomial basis functions and p the model's order i.e. the number of modes considered in the model.

The coefficients can be identified by minimising the nonlinear weighted least-squares (NLS) equation error

$$\varepsilon^{\text{NLS}}(\omega_k, \alpha, \beta) = \omega(\omega_k)\big(\hat{H}(\omega_k, \alpha, \beta) - H(\omega_k)\big) = \omega(\omega_k)\big(B(\omega_k, \beta)A^{-1}(\omega_k, \alpha) - H(\omega_k)\big) \qquad (35)$$

where ω is the scalar weighting function and $H(\omega_k)$ is the measured FRF. The equation errors are combined in a scalar cost function

$$l^{\text{NLS}}(\alpha, \beta) = \sum_{output} \sum_{k=1}^{N} tr\{(\varepsilon^{\text{NLS}}(\omega_k, \alpha, \beta))^H \varepsilon^{\text{NLS}}(\omega_k, \alpha, \beta)\} \qquad (36)$$

where $(..)^H$ is the complex conjugate transpose and N the number of points at which the FRF measurements are available.

This equation can be linearised by right-multiplying with the matrix A and the linear equation errors and cost function are respectively

$$\varepsilon^{\text{LS}}(\omega_k, \alpha, \beta) = \omega(\omega_k)\big(B(\omega_k, \alpha, \beta) - H(\omega_k)A(\omega_k, \alpha)\big) = \omega(\omega_k) \sum_{r=0}^{p} \big(\Omega_r(\omega_k)\beta_r - \Omega_r(\omega_k)H(\omega_k)\alpha_r\big) \ (37)$$

and

$$l^{\text{LS}}(\alpha, \beta) = \sum_{output} \sum_{k=1}^{N} tr\{(\varepsilon^{\text{LS}}(\omega_k, \alpha, \beta))^H \varepsilon^{\text{LS}}(\omega_k, \alpha, \beta)\} \qquad (38)$$

The coefficients are obtained by minimising the linear cost function which leads to a weighted linear least squares problem.

In the end, the poles can be computed for different model orders and compared together. If the difference existing between the results obtained with two consecutive model orders is small enough, the pole is declared stable. Eventually, those poles are complex values that contain the information of both the eigenfrequency and the damping and stabilisation diagrams are used to select the adequate results.

Note that with this method, negative values of damping can not be obtained so that the results can be trusted up until the critical flutter velocity. For higher airspeeds, negative damping is expected but the method is not able to compute them.

This method allows, through the stabilisation diagrams, to select the results so that unexpected features appearing in the FRF's like the buffeting of the lasers support when the airspeed becomes higher are not taken into account for the final results.

3.3 Experimental plates

As mentioned above, two plates are tested in the wind tunnel and the results are compared with the model that has been constructed in the first part of this work. Due to the uncertainty of being able to carry out the tests because of the sanitary crisis and the lockdown, it has not been possible to cut new plates. Those presented below have been re-used from a previous work on flutter characterisation. The mechanical properties are thus slightly different from the ones used to build the model.

The two tested plates are characterised by a span of 0.5m. However, 0.05m are placed within the vibration system to create the clamping boundary condition and the span that is considered is therefore $s = 0.45$m. The first plate is a rectangular one characterised by $AR = 2.25$, $\lambda = 1$ and $\Lambda = 0°$ and the second one is tapered so that the root chord that must be considered is no longer equal to 0.2m given that 0.05m of the span are inside the squeezing area. The root chord for this plate is equal to $c_r = 0.19$ and the tip chord is equal to $c_t = 0.1$ so that the plate is characterised by $AR = 3.1$, $\lambda = 0.526$ and $\Lambda = 0.149 \approx 8.54°$. With this test, the limitations of the model due to the assumption of constant root chord can be investigated. The two plates are illustrated in Fig.23.
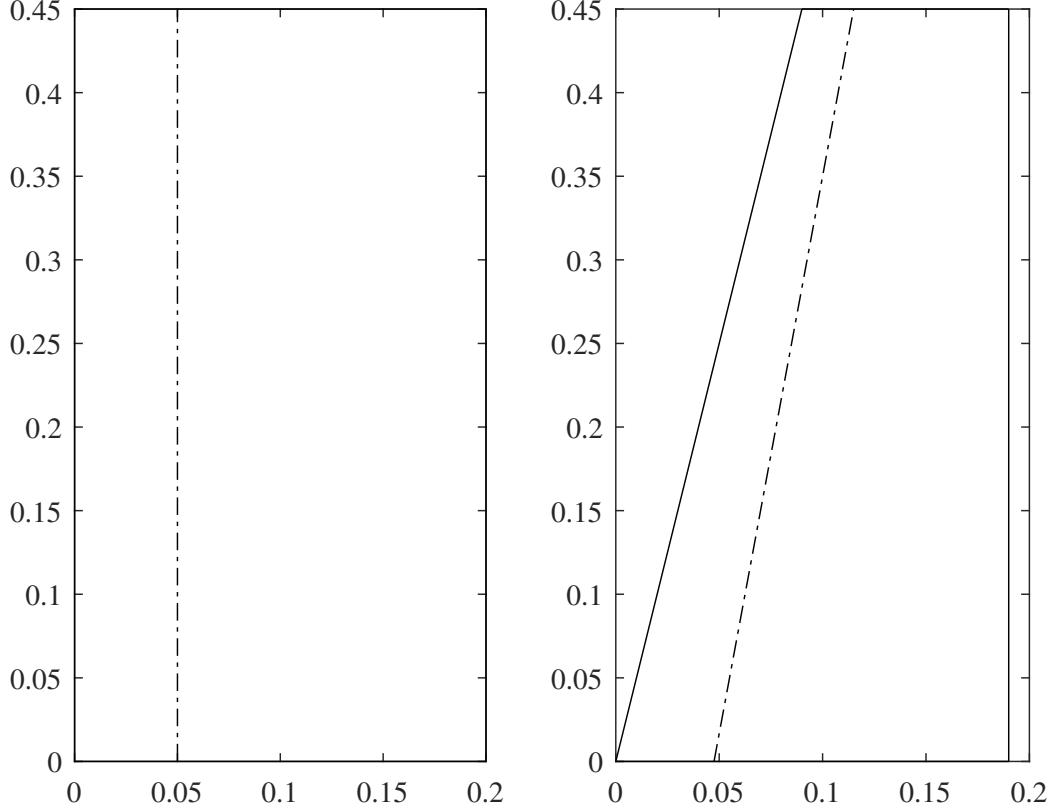
Figure 23: Experimental plates tested in wind tunnel.

To compare the experimental curves of damping and frequency to those provided by the VLM, the FE models of the two plates are required to perform the numerical modal analysis. The validity of those models is assessed by comparing the computed eigenfrequencies to those obtained with theoretical formula and experimental measurements.

From Ref.[9], the eigenfrequencies can be obtained for a uniform beam, i.e. in bending, according to

$$f_k = \frac{1}{2\pi} \mu_k^2 \sqrt{\frac{EI}{ml^4}} \tag{39}$$

with $I = \dfrac{t \cdot c_r^3}{12}$ (m^4) the second moment of area, m (kg/m) the sectional mass and l (m) the length of the beam i.e. the span of the plate. For a clamped-free beam, $\mu_1 = 1.875$, $\mu_2 = 4.694$ and $\mu_3 = 7.855$ so that the three first theoretical eigenfrequencies of bending obtained for the experimental plate 1 are equal to $f_1 = 4.061$Hz, $f_2 = 25.35$Hz and $f_3 = 71.28$Hz. Note that the formula holds for uniform beams only so that the eigenfrequencies of the tapered plate can not be computed.

The FE models are constructed in the exact same way as described in section 2.2, i.e. 55 spanwise and 40 chordwise shell elements of 0.001m thickness are used. The first five eigenfrequencies obtained for the two models are collected in Tab.7

	Experimental plate 1	Experimental plate 2
$f_1(Hz)$	4.18 (1st bending)	4.98 (1st bending)
$f_2(Hz)$	19.63 (1st torsion)	27.23 (2nd bending)
$f_3(Hz)$	26.03 (2nd bending)	34.11 (1st torsion)
$f_4(Hz)$	63.28 (2nd torsion)	73.49 (3rd bending)
$f_5(Hz)$	73.15 (3rd bending)	90.14 (2nd torsion)

Table 7: First five eigenfrequencies obtained with the FE models of the two experimental plates.

Comparing the theoretical eigenfrequencies with those obtained using the FE model of plate 1, the errors for the three first bending modes are respectively $\varepsilon_1 = 2.85\%$, $\varepsilon_2 = 2.61\%$ and $\varepsilon_3 = 2.56\%$. To complete the modal analysis of the plates and the assessment of the FE models quality, experimental measurements are taken without wind. To do so, the plunge DoF of the cart is blocked to ensure that the root of the plates are fixed. Four hammer impacts are used to excite the structure and those are made so that both bending and torsion are activated. However, it appeared that for modes higher than the third one, this excitation is not adapted so that mode 4 and 5 have not been obtained in practice. The signal being analysed in the frequency domain, the experimental eigenfrequencies are collected in Tab.8.

	Experimental plate 1	Experimental plate 2
$f_1(Hz)$	3.8 (1st bending)	4.62 (1st bending)
$f_2(Hz)$	19.31 (1st torsion)	26.69 (2nd bending)
$f_3(Hz)$	24.4 (2nd bending)	33.87 (1st torsion)

Table 8: First three eigenfrequencies obtained with the experimental measurements for the two experimental plates.

As expected, a difference exists between numerical and experimental results. The material used for the experimental tests has slightly different properties than that used for the numerical simulations. The problem is that the experimental material's properties are not well known given that the plates come from previous work and they have already been tested which can have modified their internal

structure. Nevertheless, the difference between the experimental and numerical results remaining quite small (a maximum difference of 9% is obtained for the first mode of the first plate), the FE models are eventually validated with respect to the theoretical and practical results.

3.4   Measurements validation

The system is controlled with an acquisition software developed by V2I. The measurements are taken using an accelerometer fixed on the cart and two lasers that measure the displacement of the plate. It is therefore of prior importance to assess the validity of the measurements taken by the lasers. To do so, the signal provided by the lasers when measuring the displacements of the cart are compared to that of the accelerometer. More precisely, it is their FRF's that are compared. The shaker delivers a force that is measured at the same location as the acceleration. When the Fourier transforms of each signal has been computed, the FRF's are defined as

$$H(\omega) = \frac{Y(\omega)}{X(\omega)} \tag{40}$$

where $Y(\omega)$ is the output signal in frequency domain, i.e. the signals provided by the lasers or the accelerometer in this context, while $X(\omega)$ is the input signal in the frequency domain, i.e. the force delivered by the shaker.

In the frequency domain, the displacement and the acceleration are related as follows

$$\ddot{X}(\omega) = -\omega^2 X(\omega) \tag{41}$$

so that taking Eq.40, the FRF's of the displacement measured by the lasers and that of the acceleration measured by the accelerometer are linked as

$$H_{\ddot{X}}(\omega) = -\omega^2 H_X(\omega) \tag{42}$$

With this being said, the two FRF's are compared in absolute values in Fig.24 with the FRF of the displacement multiplied by the circular frequency to the square.

The excitation delivered by the shaker is not very good at low frequencies which explains the unexpected variations observed below 5Hz. For the rest of the curve, the two FRF's are almost exactly the same. The proof is therefore made that the lasers provide the same information as the accelerometer and the validity of the measurements taken for the rest of this work is confirmed.
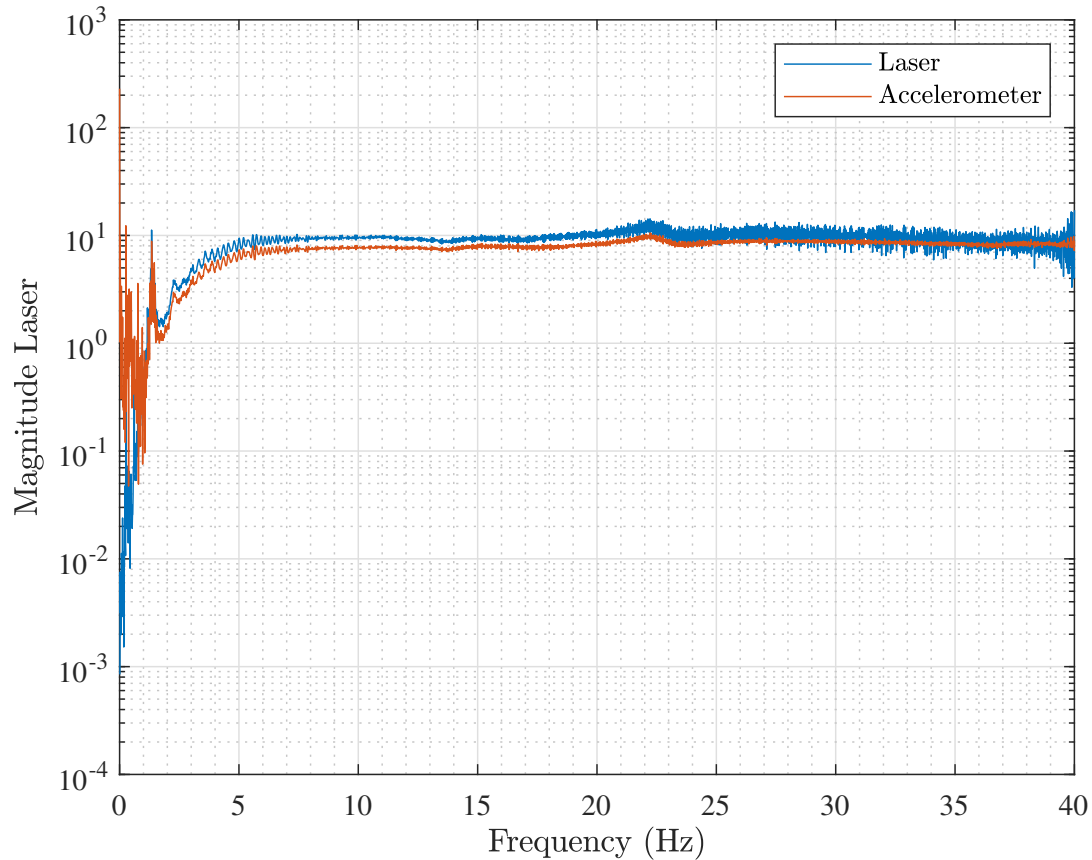
Figure 24: Comparison of the FRF's obtained from the signal provided by the lasers and that of the accelerometer.

3.5 Sensitivity to the acquisition parameters

Several parameters are not fixed in the acquisition system. Indeed, the amplitude of the signal delivered to the shaker is limited by the maximum allowable motion of the cart but different possibilities remain. Also, the acquisition frequency and time are expected to have an impact on the results which has to be evaluated to make a proper selection on the input parameters. This evaluation is achieved on the first plate in wind off conditions.

Five levels of amplitude are allowed for the input signal's voltage. Having a too high voltage results in a high motion amplitude so that the cart could hit the edges of the circular upper plate's rectangular hole. Additionally the amplitude has to be high enough to get significant displacements that can be measured correctly by the lasers but the higher the amplitude, the higher the risk to encounter undesired nonlinear phenomenon. The FRF's corresponding to the five levels are shown

in Fig.25.
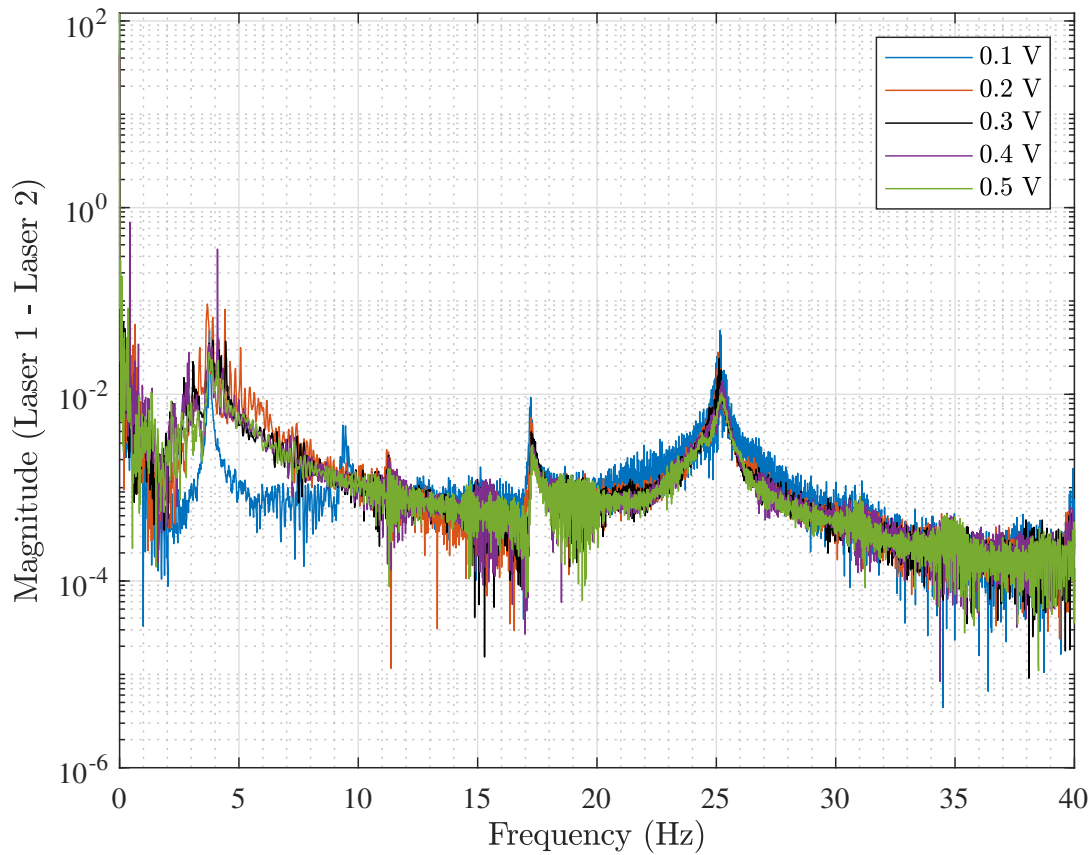
Figure 25: Comparison of the FRF's obtained with the five levels of amplitude of the input signal delivered to the shaker.

No significant nonlinear phenomenon appears no matter the amplitude of the signal. In the end, it is the amplitude of 0.3V that is selected given that the peaks at the three eigenfrequencies appear clearly enough and the corresponding FRF seems to be the one having the less noise.

Several acquisition frequencies can be used among which specific ones are proposed by the software that correspond to the clock frequencies of the acquisition card. To determine whether those specific frequencies are necessary to obtain good results or not, a comparison is made between the results obtained for two clock frequencies of the acquisition card 1651.61Hz and 2048Hz and those obtained with a random frequency 1000Hz. The comparison is again made on the basis of the FRF's and is illustrated in Fig.26.
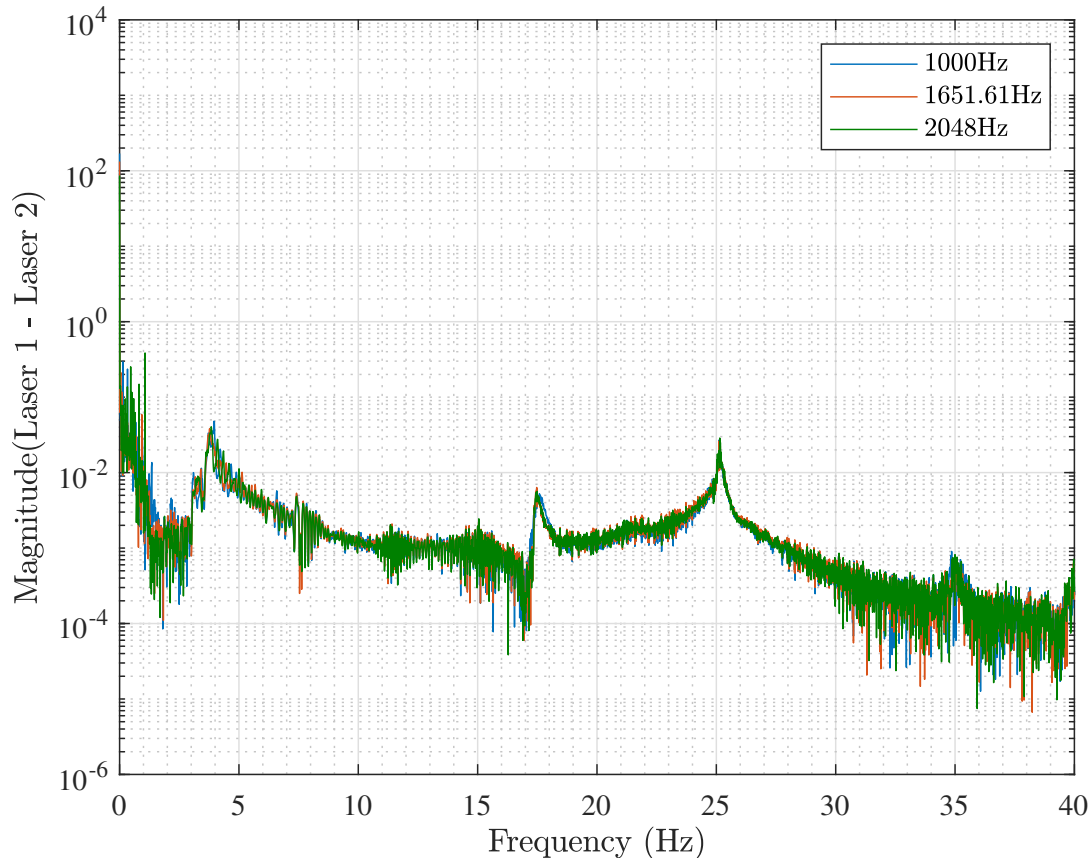
Figure 26: Comparison of the FRF's obtained with the three different acquisition frequencies.

The three FRF's are almost the same and conclusion is therefore made that for the present experiments, the difference between the selected acquisition frequency has a negligible impact on the results. For the rest of the work, it is set to $f_{\mathrm{acq}} = 2048\mathrm{Hz}$.

Finally, the duration of the sine sweep could also have an impact on the quality of the results. Accuracy is needed but it is necessary to avoid taking too much time for each test when it is not necessary. The FRF's obtained with a long test (20s for each frequency of the sweep), a medium one (2s for each frequency) and a short one (1s for each frequency) are compared in Fig.27.
The results appear to contain more noise for the longest test so that taking too much time for each frequency does not bring useful additional information. The two other tests look pretty much the same eventhough the shortest one seems to encounter more troubles when reaching higher frequencies. In the end, it is chosen to spend 2s for each frequency of the sine sweep.

It is interesting to note that eventhough the excitation system provides an excitation that is way
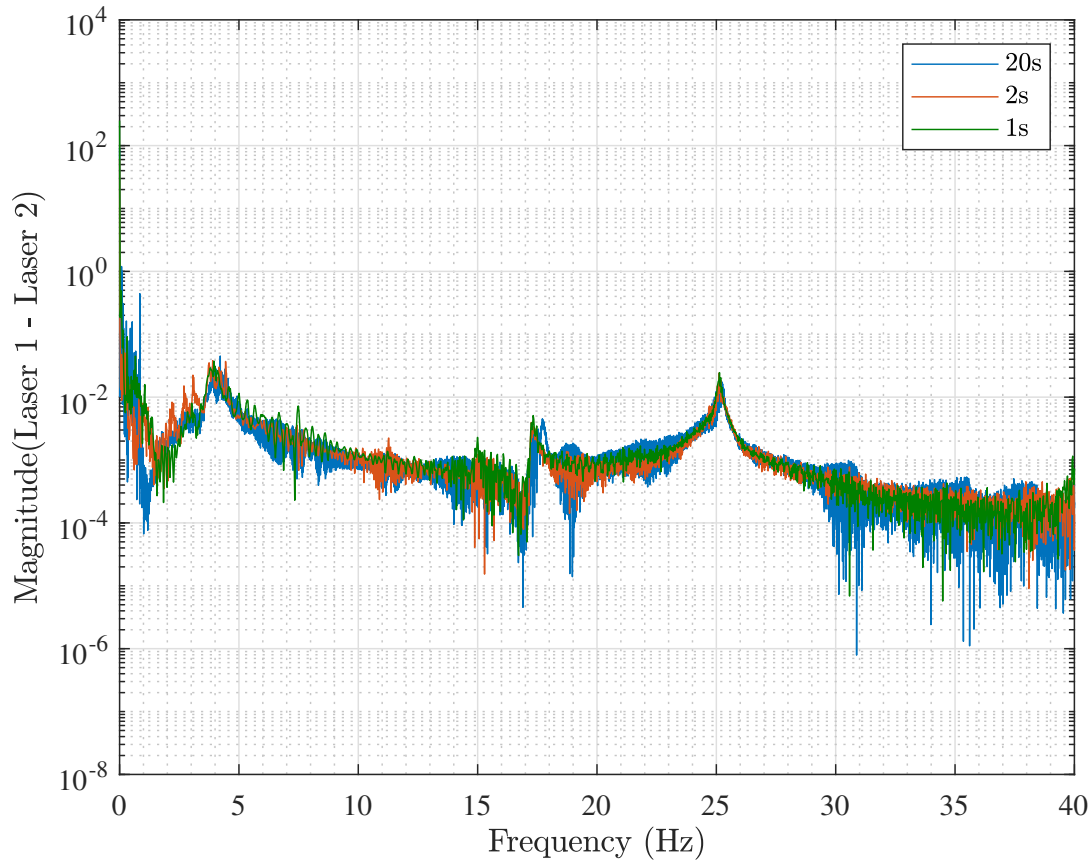
Figure 27: Comparison of the FRF's obtained for three values of the time spent on each frequency.

more accurate than that used for previous works on the same topic that consisted in an impulse provided with a rope attached to the trailing edge that was vigorously pulled, the temporal and frequency-domain signals are of similar quality. A first thing that could explain this issue is that the same lasers of range 0.5m have been used for the measurements and conclusion could be drawn that they are not accurate enough to get a cleaner signal even with a better way of exciting the structure. They would therefore be the limiting part of the setup. Also, as mentioned in the introduction of the experimental comparison, the sanitary crisis prevented the tests to be checked properly. The excitation system had to be tested alone within a short period of time so that its quality could be poorer than expected and the lack of time prevented to check and solve all the possible problems. Among those problems, the rod connecting the shaker to the cart was not perfectly perpendicular to the cart so that the excitation was a bit out of alignment. Consequently, an unexpected friction has been observed between the cart's bearings and the cylindrical supports and the damping was higher than expected. Finally, the excitation is only made in plunge so that the torsion mode is not directly excited in wind off conditions making it less visible in the curves.

The same goes for the tested plates that should have been new ones but the situation was such that no time could be wasted for that and older plates of probably poorer quality had to be tested.

3.6   Wind on results.

In this section, the tests at increasing airspeeds are carried out. The goal is to get the frequencies and dampings for each tested speed and plot them to get the curves predicting the flutter.

Three equal tests have been performed for both wings for redundancy and the airspeed is measured using a Pitot tube. In the end, the experimental curves are obtained and compared with those predicted by the VLM code and illustrated respectively for the rectangular and tapered plate in Figs.28 and 29
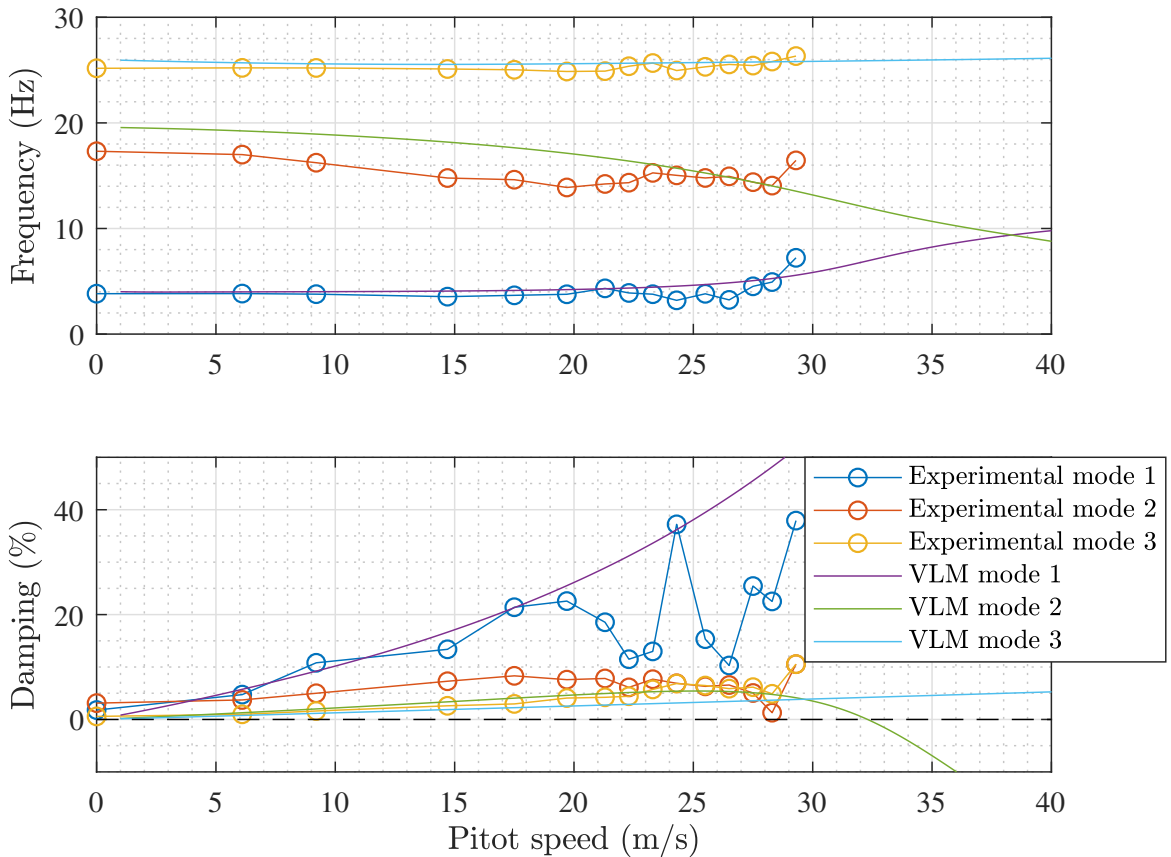
Figure 28: Experimental and numerical frequency and damping curves obtained for plate 1 with configuration $AR = 2.25$, $\lambda = 1$ and $\Lambda = 0$.

When analysing the curves, it must be kept in mind that as mentioned above, the experimental
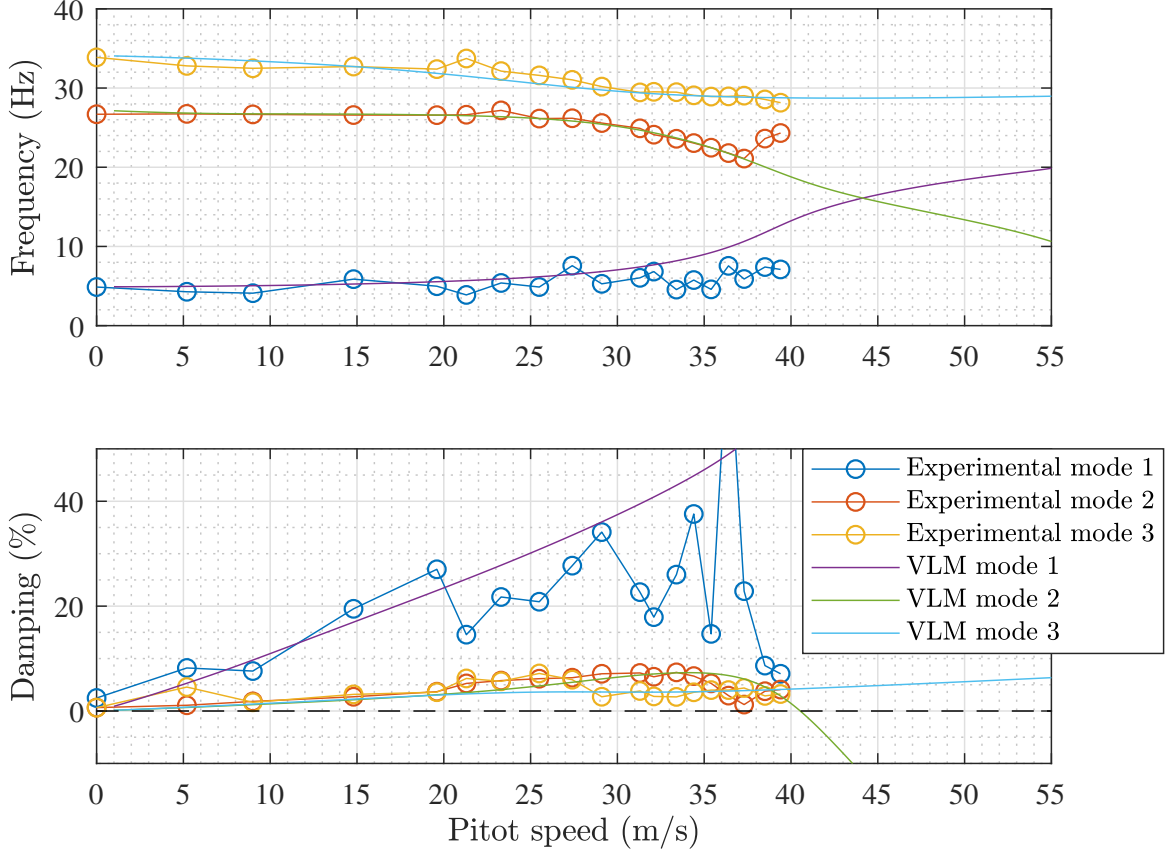
Figure 29: Experimental and numerical frequency and damping curves obtained for plate 2 with configuration $AR = 3.1$, $\lambda = 0.526$, $\Lambda = 0.149$ and $c_r = 0.19$.

plates do not have the same mechanical properties as those used for the numerical simulations. Additionally, those plates have already suffered from shocks (rope pulling) which could have locally modify the internal structure. Finally, the support of the lasers is fixed to the ceiling of the wind tunnel meaning that its end is not attached. Therefore, when the airspeed becomes high enough, it starts oscillating which can pollute the measured signal making the analysis less obvious.

- **Plate 1**

With this plate, the mode that is fluttering is the first torsion one, i.e. the second mode. About the variation of the frequency with the airspeed for the first plate, the experimental results are pretty well matching the numerical curves for the first and third modes. Concerning the torsion, the tendency of the curves is the same but the experimental results are lower by almost a constant value that is the difference between the numerical and the experimental wind-off natural frequen-

cies. However, when the airspeed reaches 23.3m/s, the experimental points come closer to the VLM curve. The excitation is only made in plunge so that only the bending modes are activated correctly, the torsion needs an external load namely the aerodynamic one in this context to be activated. The matching of the curves could therefore result from the airspeed that became high enough for a proper activation and thus a proper measurement of the torsion.

Concerning the damping curves, for low airspeed, the results for the first and third modes are close to the numerical ones. Below 19.7m/s, the maximum difference in the damping percentage is 2.9% for mode 1 and 1.55% for mode 3. When considering higher airspeeds, the damping obtained for the first mode is expect to increase rapidly. However, in a practical context, this means that the response is highly damped so that the correct identification of the first mode becomes more difficult which could explain the weird variations between two consecutive airspeeds. For the third mode, the dampings are always slightly overestimated but the experimental and numerical curves are following the same tendency. Concerning the second mode, the experimental results are overestimated for almost all the airspeed range. Nevertheless, the general tendency is exactly the same. The differences could result from the difference existing between the experimental and numerical plates properties.

The last experimental point, obtained at airspeed $V = 29.3$m/s, is diverging from the general tendency. This result therefore shows that something occurred and in fact, the plate is fluttering. As expected, the Polymax method is not able to compute the negative damping so that the results are no longer reliable for higher airspeeds. The critical flutter speed is located between 28.3m/s and 29.3m/s. The damping obtained for $V = 28.3$m/s is equal to 1.3% so that the flutter speed is very close to that point. Given that no additional information is available and that a regression curve between the points provides a flutter speed above $V = 29.3$m/s which is not realistic, it has been decided to fix the experimental flutter speed for the first plate to $V_{\text{f,plate1}} = 28.3$m/s. Consequently, the experimental flutter frequency is equal to $f_{\text{f,plate1}} = 14.06$Hz and the flutter index can be computed

$$V_{\text{f,plate1}}^* = \frac{28.3}{0.1 \cdot 14.06} = 20.128 \tag{43}$$

- **Plate 2**

With the second plate, it is the second bending mode that encounters flutter which again corresponds to the second vibration mode. No constant difference appears between the experimental and numerical results for the frequency curves. Moreover, except for the first mode at higher air-

speeds, the results are very close to what was expected even for the torsion mode while a significant difference was observed for the previous plate.

For the damping curves, again the results for the first mode starts variating a lot when reaching 21.3m/s. For the second and third modes respectively corresponding to second bending and first torsion, the experimental damping follows pretty well the numerical predictions up until $V = 19.6$m/s. After this airspeed, the values suddenly slightly jump up but keep following the same tendency as what is expected.

Here, two post-critical tests have been performed so that the two last points correspond to fluttering ones and do not bring meaningful information for the present work. For this plate, it is possible to build a 5th order polynomial using the points before flutter that gives an approximation of the exact experimental critical flutter speed shown in Fig.30.
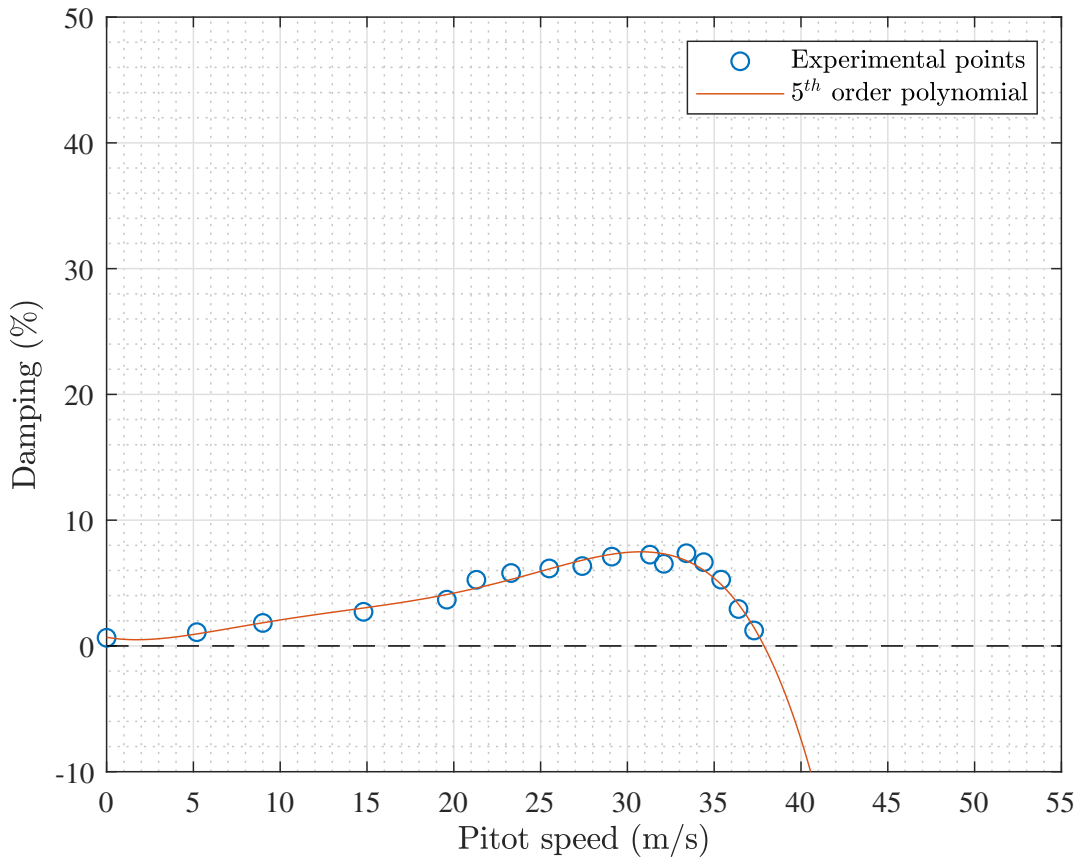

Figure 30: Experimental damping obtained for the second mode of plate 2 fitted with a 5th order polynomial.

Such a polynomial crosses the zero damping axis at $V_{\text{f,plate2}} = 37.87$m/s which corresponds to a

flutter frequency equal to $f_{\text{f,plate2}} = 20.47$Hz. Note that this plate has the specificity to have a root chord that is not the same as all the plates considered until here. The goal was to investigate the limitation imposed by the constant root chord assumption and therefore the flutter index is

$$V^*_{\text{f,plate2}} = \frac{37.87}{0.095 \cdot 20.47} = 19.474 \tag{44}$$

3.7   Comparison with the model's prediction

First of all, the experimental results can be compared to those provided by the VLM. This comparison is made in Tab.9

	Plate 1		Plate 2	
	$\mathbf{V}_f$ (m/s)	$\mathbf{f}_f$ (Hz)	$\mathbf{V}_f$ (m/s)	$\mathbf{f}_f$ (Hz)
VLM	32.3	11.97	40.5	18.4
Experimental	28.3	14.06	37.87	20.47
Difference (%)	12.38	14.86	6.49	10.11

Table 9: Comparison of the flutter speed and frequency obtained from VLM and from the experiments in wind tunnel for both the rectangular (1) and the tapered (2) plates.

Again, the differences existing between the experimental plates properties and those used for the numerical simulations are likely to be a major cause of the observed differences in the results. Nevertheless, those errors all remain below 15% which can still be considered as a relatively small error. The problem here is that the VLM slightly overestimates the flutter speed while for safety, underestimating it would probably be a better solution for building a flight envelope where flutter shall never appear.

The experimental results in terms of the flutter index can be compared to the model that has been built in this work. None of the plates activate the hump mode so that the flutter index is given by Eq.32 and the model results are

$$\begin{cases} V^*_f = 26.51 & \text{for plate 1} \\ V^*_f = 22.19 & \text{for plate 2} \end{cases} \tag{45}$$

The difference between the experimental and theoretical flutter indices are respectively equal to 6.382 and 2.716 which corresponds respectively to 24.07% and 12.24%. The differences existing between the VLM and the experimental speeds and frequencies combine when computing the flutter indices moving them further from each other. Surprisingly, it is the plate that does not verify the condition of $c_r = 0.2$m that is the closest to the model results so that this modification seems to alleviate the contrast between the numeric and the experiment.

Looking at those experimental results only, the model built on the basis of numerical simulations can not be validated. Nevertheless, with all the limitations existing on the experimental setup due to lack of time, this model can not be concluded inaccurate neither. More verification with wind tunnel tests should be carried out to conclude properly on the validity of the model for a practical application.

4 Conclusion

The goal of this master thesis was to provide a mathematical model predicting the flutter index of flat cantilever plates on the basis of numerical results obtained with the Vortex Lattice Method. To this purpose, the dependency of the flutter phenomenon on three geometrical parameters of the wings namely the Aspect Ratio, the taper ratio and the quarter-chord sweep angle has been investigated. The thickness, the root chord and the material properties have been kept constant and no camber has been considered. The design domain has been first divided into four levels for each of the three factors generating a starting set of 64 plates. Those plates have been modelled on NX and a modal analysis was performed using the solver NASTRAN to get the eigenmodes and the stiffness and mass matrices required in the VLM. Then, the numerical simulations have been carried out and the flutter indices have been computed and plotted as a function of the three geometrical parameters.

With this plot, it appeared that an unexpected phenomenon occurred creating a sudden drop of the flutter indices values for a certain portion of the design domain. This phenomenon has been called hump mode activation and results from the fact that under certain geometrical conditions, the third mode damping curve featured a hump that crossed the zero axis before going back to positive values before the classical bending-torsion flutter occurs. The critical flutter mode therefore changed suddenly. Consequently, following its definition, the flutter index values were suddenly decreasing creating a discontinuity in the results. The activation of the hump mode has then been

investigated and an attempt to explain its appearance has been proposed. Finally, this activation has been modelled as a discontinuity straight line dividing the design domain into two distinct zone whose variation is given by Eq.11. The consideration of the hump mode on the design domain is limited to a maximum sweep angle of $\Lambda = 0.27376 \approx 15.6°$ given that above this value, the damping curves of the second and third modes switch their critical points eventhough the hump mode is still active.

Then, the linear regression theory has been used separately for the two zones of the domain. Three different models have been tested namely a simple first order polynomial, a second order polynomial with interaction terms only and a complete second order polynomial. Use has been made of the least-squares estimates to get the model's coefficients which required to have a model's matrix of full rank. It appeared that for the zone after the hump activation, this matrix was not of full rank for the complete second order model and the term corresponding to Λ^2 had to be removed. The three models have then been compared in terms of maximum residuals and multiple correlation coefficient R^2 and as expected the second order model was the closest one to the numerical results. In the end, starting from this model, a backward elimination has been carried out to remove all the terms that did not bring significant information. The final model described by Eqs.31 and 32 was ensuring maximum residuals of 2.17% and 3.22% and multiple correlation coefficients of $R^2 = 0.9936$ and $R^2 = 0.9914$ respectively for the zone before and after the hump activation ensuring that the model is highly reliable within the design domain.

With the final model being established, it is possible to determine which parameters are influencing the most the flutter phenomenon. For the zone where the hump is not active, it is the second mode that is responsible of flutter. For this zone, it is the taper ratio and the aspect ratio that are the main factor responsible of the flutter respectively under the linear and the quadratic forms. The critical flutter index mainly vary as a linear function of λ but curvature is needed in terms of AR which appears clearly in Fig.21. With the root chord being kept constant, from Eqs.1 and 2, it is consequently the tip chord and the span of the plate that dominate the flutter characterisation. The less important term corresponds to the sweep angle under its quadratic form showing that V_f^* is mainly varying linearly with Λ. For the zone where the hump mode is the critical one, the two most important term corresponds to the aspect ratio under both its linear and quadratic forms showing again that the span is of prior importance for characterising flutter. The less important term corresponds to the interaction between the taper ratio and the sweep angle.

Eventhough the sweep angle does not represent the main factor influencing the critical flutter in-

dex for the two zone separately, it takes a major role in the apparition of the hump mode and to determine its zone of validity. As a consequence, under its linear form, the sweep angle is of major importance for modelling correctly the phenomenon.

To validate the model, two experimental tests have been carried out in the wind tunnel of the UNIVERSITY OF LIEGE using an excitation system in plunge. The sanitary crisis prevented those tests to be carried out as accurately as expected so that some potential sources of difference could not be investigated. Those potential sources are the plates having not well known mechanical properties to which is added the fact that they had already been tested for previous works and as a consequence their characteristics could already have been modified. Also the excitation system has not been checked properly before starting the tests, the lasers used to measure the displacements of the plate were not perfectly accurate so that the temporal and frequency domain signals were not so clean. Finally, the support for the lasers was fixed to the wind tunnel ceiling so that it started vibrating with the airflow becoming more important. The frequencies and dampings curves obtained with the experimental tests have then been compared to the curves provided by the VLM showing that they were following the same tendency eventhough some constant difference were sometimes appearing. In terms of flutter speeds and frequencies, the experimental results were quite close to those expected from the VLM and a maximum difference of order 15% has been observed for flutter frequency of the rectangular plate. Finally, the flutter indices from both numerical simulations and experimental tests have been compared. The differences for the two plates were of order 24.07% and 12.24% respectively for the rectangular and the tapered one due to the combination of the differences observed for both the speed and the frequency. Consequently the model could not be validated for the practical tests. Nevertheless, with the potential sources of difference and error mentioned above that have not been checked and solved, the model could neither be said not valid neither. Note that only the zone before the hump activation has been checked so that no conclusion can be drawn for the other one. Finally, despite the impossibility of drawing a proper conclusion about the model, it is very likely that the VLM would provide results that are close to those measured in wind tunnel when the errors will be solved.

4.1 Improvements and future work

For future work, the first task that could be achieved is a proper investigation of the hump mode activation in order to understand correctly the reasons of its appearance. Its existence could there-

fore be deleted allowing the critical flutter speed to be increased. Also, it might be useful to select test cases that are beyond the limits of the design domain selected here to verify is the model is valid for any input values and if the limitation of the hump mode activation proposed here is true no matter the configuration. Moreover, this work could be used as a basis for completing the model with all the parameters that have been kept constant. A new regression analysis could be used with the material properties and the thickness varying while keeping the aspect ratio, taper ratio and the sweep angle constant. The results would then be added to those presented here to complete the model. Finally, given that the VLM is able to deal with camber, its dependency can also be investigated so that the final model would therefore be adapted for flutter characterisation of classical wings. With a model comprising those parameters, the troubles observed with the experimental plates could be alleviate given that any type of material could be modelled so that there would be less restriction for the experimental tests.

Concerning the practical validation, major improvements can be made. First of all, it has been observed that the excitation system was not perfect. The excitation was not delivered perfectly parallel to the axis of the linear bearings bringing an excessive amount of friction. A correction of the excitation direction could help for getting cleaner signals and for a better identification of the vibration modes. Also, new plates with well known properties should be cut to conduct a proper validation with respect to the numerical work. Concerning the measurement system, the lasers used were limited in range so that they had to be kept near the plates which could have modified the airflow around the plates. Having a larger range of detection would be useful to remove the lasers away from the system and avoid unwanted interaction. More accuracy in the signal could also be appreciated for properly identify the modes of interest and maybe capture those at higher frequencies. Finally, attaching the lasers support to both end at the ceiling and the floor of the wind tunnel should prevent its vibration when the airspeed becomes large enough. This should result in a better identification of the vibration modes.

For future work, it is necessary to test plates that have configurations located on both sides of the discontinuity line characterising the activation of the hump mode. In this work, only the zone where it is not active has been tested and experimental tests covering the whole design domain are needed to perform a proper validation of the numerical results. Finally, once the practical issues are corrected, with experimental tests covering the selected design domain, a correction could be brought to the numerical model so that it would represent the real phenomenon with more accuracy.

APPENDIX

58

A Modal extraction from NX

The software NX Nastran provides the modal characteristics of any model but the extraction of these data is not obvious. Here is a brief summary of the procedure followed in this paper

A.1 NX Nastran

- First simulation: once the wing is modelled and mapped with finite elements, the modal analysis can be performed.

  ▹ Select the "Real eigenvalues" solution type.

  ▹ Fix the nodes that have to be clamped.

  ▹ Select "Edit solution attributes", go to "Bulk data", parameter "EXTEOUT" and set it to "DMIGPCH". This will create a punch file containing the stiffness and mass information for each node.

  ▹ Once the simulation is complete, save the punch file as a text file to be processed easily.

- Second simulation: the nodal displacements and coordinates have to be extracted.

  ▹ "EXTEOUT" is set back to "none".

  ▹ Once the simulation is achieved, select the displacements mode by mode. Click on "identify results" and "select all". Then click on the option "Export selection to a file (.csv)". This creates a file containing the nodal displacements and coordinates.

A.2 MatLab

In this work, all the data are processed using MatLab.

- save the csv file containing the nodal coordinates and displacements as a matrix

  ▹ 2nd column contains the x-coordinates with respect to the origin of the coordinate system of NX

  ▹ 3rd column contains the y-coordinates with respect to the origin of the coordinate system of NX

  ▹ 4th column contains the z-coordinates with respect to the origin of the coordinate system of NX

  ▹ 5th column contains the x-displacements

- ▸ 6th column contains the y-displacements
- ▸ 7th column contains the z-displacements

- The punch file is presented under columns form.

  - ▸ If the first column is "DMIG* KAAX" or "DMIG* MAAX" then the following column gives the concerned node's group of columns respectively in the stiffness and mass matrix (each node has 6 columns, one for each dof).

    In this case, the third column of the punch file corresponds to the component out of the group of 6 columns.

    Example: if the line line is "DMIG* KAAX 2 5" then in the stiffness matrix, it is the 5th column out of the 2nd group of 6 columns that is concerned. This corresponds to the 11th column of the matrix.

  - ▸ If the first column is "*" then the following number indicates the node's group of lines that is concerned. Then the third column corresponds to the component out of the group of 6 lines and the fourth one is the value to be assigned at the column and line that have been specified.

    Example: if the line is "* 1 2 1.3105E+08" then it is the 2nd line of the 1st group of 6 lines that is concerned (i.e. the 2nd line of the matrix) and the value to be assigned is $1.3105 \cdot 10^8$.

  - ▸ Once this is done, the symmetry of the matrix has to be taken into account so that the same value must be assigned at the symmetric location.

  - ▸ Finally, attention must be paid to the fact that the clamped node are also taken into account in the matrices making them singular.

References

[1] Michael W. Kehoe , October 1995. *A Historical Overview of Flight Flutter Testing.* , NASA Technical Memorandum 4720

[2] Dennis J. Martin, Langley Aeronautical Laboratory Langley Field, Va. , February 1958. *Summary of flutter experiences as a guide to the preliminary design of lifting surfaces on missiles.* , National Advisory Committee for Aeronautics , technical notes 4197

[3] Joseph Katz, Allen Plotkin, 1991. *Low-speed Aerodynamics. From Wing Theory to Panel Methods.* , McGraw-Hill Series in Aeronautican and Aerospace Engineering

[4] G. Dimitriadis, N.F. Giannelis, 2017. *A modal frequency-domain generalised force matrix for the unsteady Vortex Lattice method.* , Journal of Fluids and Structures

[5] Jonsson Eirikur, Riso Cristina, Lupp Christopher, Cesnik Carlos, Martins Joaquim, Epureanu Bogdan, 2019. *Flutter and post-flutter constraints in aircraft design optimization.* , Progress in Aerospace Sciences

[6] Raymond H. Myers, Douglas C. Montgomery, Christine M. Anderson-Cook, 2016. *Response surface methodology: Process and product optimization using designed experiments.* , Fourth edition.

[7] Walter Tinsson, 2010. *Plans d'expérience: constructions et analyses statistiques.* , Mathématiques & Applications.

[8] Douglas M. Bates, Donald G. Watts, 1988. *Nonlinear regression analysis and its applications.*

[9] Michel Géradin, Daniel J. Rixen, 2015. *Mechanical Vibrations: Theory and Application to Structural Dynamics.* , Third edition

[10] B. Peeters, M. El-kafafy, P. Guillaume, 2012. *The new PolyMAX Plus method: confident modal parameter estimation even in very noisy cases.*